Journal of Fluids and Structures 95 (2020) 102997

Contents lists available at ScienceDirect

Journal of Fluids and Structures

journal homepage: www.elsevier.com/locate/jfs

Transverse vortex-induced vibration of a circular cylinder on a viscoelastic support at low Reynolds number

Rahul Mishra [a,b,c,*], Atul Soti [b], Rajneesh Bhardwaj [c], Salil S. Kulkarni [c], Mark C. Thompson [d]

[a] IITB-Monash Research Academy, IIT Bombay, Mumbai, 400076, India
[b] Department of Aerospace Engineering, IIT Kanpur, Kanpur, Uttar Pradesh, 208016, India
[c] Department of Mechanical Engineering, IIT Bombay, Mumbai, Maharashtra, 400076, India
[d] Fluids Laboratory for Aeronautical and Industrial Research (FLAIR,) Department of Mechanical and Aerospace Engineering, Monash University, Clayton 3800, Australia

ARTICLE INFO

Article history:
Received 13 September 2019
Received in revised form 14 February 2020
Accepted 3 April 2020
Available online 16 April 2020

Keywords:
Vortex-induced vibration
Damping
Viscoelasticity
Low Reynolds number flow

ABSTRACT

The effect of a viscoelastic-type structural support on vortex-induced vibration (VIV) of a circular cylinder has been studied computationally for a fixed mass ratio ($m^* = 2.546$) and Reynolds number ($Re = 150$). Unlike the classical case of VIV where the structural support consists of a spring and damper in parallel, this study considers two springs and one damper, where the two springs are in parallel and the damper is in series with one of the springs. This spring/damper arrangement is similar to the *Standard Linear Solid* (SLS) model used for modelling viscoelastic behaviour. The viscoelastic support (SLS type) is governed by the following two parameters: (a) the ratio of spring constants (R), and (b) the damping ratio (ζ). The focus of the present study is to examine and understand the varied response of the cylinder to VIV as these parameters are varied. For small ζ and R, the cylinder response shows characteristics similar to the classical case, where the amplitude response is composed of an upper- and the lower-type branch. The presence of upper-type branch at low Re is evident through the peak lift force, frequency and phase response of the cylinder. As the damping ratio is increased, the vibration amplitude decreases and hence the upper-type branch disappears. There exists a critical value of $\zeta = 1$ beyond which the amplitude again increases asymptotically. The non-monotonic variation of amplitude response with ζ is presented in the form of the "Griffin plot". The amplitude, force, frequency and phase-difference response of cylinder were found to be mirror symmetric in $\log(\zeta)$ about $\zeta = 1$. In addition, the effect of R at the critical value of damping, $\zeta = 1$, was studied. This show that the amplitude decreases with an increase of R, with suppression of the response branches for high R values. The results suggest that a careful tuning of the damping may be effectively employed both to enhance power output for energy extraction applications or to suppress flow-induced vibration.

1. Introduction

Vortex-induced vibration of a cylinder, and in particular the case where a rigid circular cylinder is elastically mounted and constrained to oscillate transversely to a free stream, has been well-studied and reported on, as can be seen

* Corresponding author at: IITB-Monash Research Academy, IIT Bombay, Mumbai, 400076, India.
E-mail address: rahulmishra.iitk@gmail.com (R. Mishra).

https://doi.org/10.1016/j.jfluidstructs.2020.102997
0889-9746/

Nomenclature

Δf_n^*	Increment in frequency for hysteresis computation.
ν	Kinematic viscosity of the fluid
ρ	Fluid density
ζ	Damping ratio ($= c/2\sqrt{km}$)
$A^*_{y,max}$	Amplitude of cylinder oscillation
c	Damping coefficient
C_A	Added mass coefficient for transverse oscillations in still fluid, $C_A = 1$ for circular cylinder
C_L	Lift force per unit length of cylinder along transverse direction ($= 2F_y/\rho U_\infty^2 DL$)
D	Cylinder diameter
f_n	Structural natural frequency based on k ($= \frac{1}{2\pi}\sqrt{k/m}$)
f_v	Natural vortex shedding frequency of a non-oscillating cylinder
F_y	Force exerted on cylinder in the transverse direction
f_y	Transverse oscillation frequency of cylinder
F_{int}	Internal force due to spring–damper system.
f_s	Structural natural frequency of system
k	Equilibrium stiffness of the spring
k_n	Non-equilibrium stiffness of the spring
m	Mass per unit length of cylinder
m^*	Mass ratio per unit length of cylinder ($= 4m/\pi\rho D^2$)
R	Ratio of non-equilibrium stiffness to equilibrium stiffness of the spring, ($= k_n/k$)
Re	Reynolds number ($= U_\infty D/\nu$)
U_∞	Free stream velocity
U_r	Reduced Velocity ($= U_\infty/f_s D$)
Superscript $*$	Represents nondimensional quantity

from comprehensive reviews of Sarpkaya (1979), Bearman (1984), Parkinson (1989), Sarpkaya (2004), Williamson and Govardhan (2004, 2008), Bearman (2011) and Wu et al. (2012). Vortex-induced vibration (VIV) occurs when vortex shedding exerts an oscillatory or quasi-oscillatory force on a structure causing it to vibrate. Indeed, elastically mounted structures near resonance develop flow-induced oscillations by extracting energy from the flow. In turn, the oscillations of the structure modify the flow and give rise to a coupled nonlinear interaction.

In general, the VIV response of a circular cylinder in uniform flow is dependent on the Reynolds number, the mass ratio, the damping ratio and the reduced velocity. The Reynolds number is defined as $Re = U_\infty D/\nu$, where U_∞ is the free stream velocity, D is the cylinder diameter and ν is the kinematic viscosity of the fluid. The mass ratio is defined as $m^* = 4m/\pi\rho D^2$ where m and ρ are the mass per unit length and the fluid density, respectively. The damping ratio is the ratio of damping to the critical damping, given by $\zeta = c/2\sqrt{km}$, where k is the spring stiffness. Finally, the reduced velocity as defined by Sumer et al. (2006) is the ratio of the wavelength of the cylinder trajectory to its diameter and is given by $U_r = U_\infty/f_s D$, alternatively, it can be thought of as a non-dimensional structural oscillation period, hence (VIV) resonance occurs when this matches the shedding period, typically when $U_r \sim 5$ for a circular cylinder.

Most past studies have focused on one-degree-of-freedom cross-flow VIV of a circular cylinder. Vortex shedding occurs due to the presence of two separating shear layers that subsequently roll up alternately into low pressure discrete vortical structures inducing oscillation in a direction transverse to the free stream. If the vortex-shedding frequency is close to the natural frequency of the cylinder, large oscillation amplitudes occur. Indeed, such a response can occur over a wide range of reduced velocities (Bearman, 1984). This reduced velocity range over which the structure undergoes near-resonant vibration is referred to as the lock-in range. The amplitude of cylinder vibration can undergo jumps as the reduced velocity is varied, which give rise to different response branches. For a low mass-damping parameter (product of mass ratio and damping ratio, $m^*\zeta$), Khalak and Williamson (1999) experimentally found three response branches: the initial, upper and lower branches as the ratio of vortex-shedding frequency to structure natural frequency was varied (f_y/f_n). At higher $m^*\zeta$, they found only two different branches: the initial and the lower branch. These branches are identified by the jumps in the amplitude response. The maximum vibration amplitude was observed to be close to one cylinder diameter (D) in the upper branch, with a relatively lower amplitude of oscillation occurring in the lower branch. A 2S vortex shedding pattern (two single vortices shed per cycle, i.e. a von-Karman street-type wake) in the initial branch, a 2P mode (two vortex pairs of opposite sign shed per cycle of vibration) in the lower branch and a $2P^*$ mode (similar to 2P except that vortex pairs in one of the half cycles convect away from in front of the body) in the upper branch (Williamson and Roshko, 1988). At low $m^*\zeta$, the mode change between initial and upper response branches involves hysteresis, whereas intermittent switching of modes occurs at the upper and lower branch transition. Both the transition jumps also show

jumps in amplitude and frequency. The upper-to-lower branch transition is also characterized by a jump from 0° to 180° in the phase difference between lift force and displacement signals, whereas the phase difference is 0° for both the initial and the upper branch. The peak vibration amplitude is dependent on the mass-damping ratio, $m^*\zeta$, whereas the synchronization regime (measured by the range of reduced velocity U_r) is primarily determined by m^*. Khalak and Williamson (1997) showed that for high $m^*\zeta$, the frequency of cylinder oscillation (f_y) was close to structural natural frequency (f_n). At low $m^*\zeta$, f_y is higher than f_n in the synchronization regime, yet f_y remains below the vortex-shedding frequency, f_v. In the lock-in or synchronization region, the frequency of cylinder vibration was found to be same as the vortex-shedding frequency, i.e. $f_v \approx f_y$.

The majority of the numerical studies have been performed at low *Re* using two-dimensional simulations. Blackburn and Henderson (1996) presented simulation results at $Re = 250$, and showed a lower maximum amplitude of approximately 0.6*D*. They also observed a chaotic response over a range of f_n/f_v and only the regular 2S mode, implying that the 2P mode need not necessarily be associated with the large amplitude response plateau in the lock-in regime. The branching behaviour was numerically investigated by Leontini et al. (2006b) at $Re = 200$ who found two synchronous response branches that resembled the upper and lower branches, supported by instantaneous amplitude rather than peak amplitude. They also suggested that the branching at higher *Re* was not the product of three-dimensionality, which was contrary to Govardhan and Williamson (2000) who implied that the upper branch does not occur at low *Re* for two-dimensional flow. Pan et al. (2007) and Guilmineau and Queutey (2004) performed simulations for the low mass-damping case, with motion constrained to transverse oscillations to a free stream by employing a two-dimensional Reynolds-averaged Navier–Stokes (RANS) model based on the Shear-Stress Transport (SST) $k-\omega$ turbulence model. They were able to get the initial and lower branches but the results did not match the upper branch found experimentally. CFD studies of VIV of a circular cylinder have also been conducted using three-dimensional numerical models. Wang et al. (2017) investigated two-degree-of-freedom VIV of a circular cylinder with varying in-line to cross-flow natural frequency ratios at low mass-ratio ($m^* = 2$) at $Re = 500$. Gsell et al. (2016) simulated 2DOF VIV of a circular cylinder at $Re = 3900$ through direct numerical simulation of the 3D Navier–Stokes equations. Notably, the maximum transverse amplitude and structural response compared well with experimental observations. Pastrana et al. (2018) modelled VIV using large-eddy simulation (LES) at subcritical Reynolds numbers ($Re = 3900, 5300, 11\,000$).

The effects of damping on the vibration response is important as damped VIV can be harnessed for converting flow energy into electrical energy. A cylinder undergoing VIV has kinetic/potential energy that can be extracted using a power transducer such as an electromagnetic generator (Soti et al., 2017). In the past, the effects of damping on the response behaviour of the system were explored by Vickery and Watkins (1964) and Scruton (1963), who reported peak amplitudes in air and water against a mass-damping parameter ($m^*\zeta$). In early studies, Feng (1968) reported the effects of damping on both the amplitude and frequency response. They used an electromagnetic eddy-current-based damper for applying different damping values to the system of circular and D-shaped cylinders in a wind tunnel. Due to the high mass-damping parameter, the amplitude was small and there were no discontinuities; two-branch response behaviour (the initial and the lower branches) was observed. Recently, Klamo et al. (2005) studied the damped system experimentally using a controlled magnetic eddy current technique to provide variable damping, and reported that the maximum amplitudes ($A^*_{y,max}$) depend not only on damping but also on Reynolds number. Subsequently, Klamo et al. (2006) studied the effects of controlled damping on the amplitude and frequency response, and showed that a VIV system transitions from a two-branch to three-branch response as damping is varied from high to low. They also observed three distinct branches for the frequency response, analogous to that seen for the three amplitude branches. They reported hysteresis between the lower branch and the desynchronized region at low Reynolds numbers. Blevins and Coughran (2009) experimentally measured the steady-state response of the elastically supported cylinder for six values of damping, for distinct Reynolds numbers from $\mathrm{Re} \in [170, 150\,000]$. They observed monotonic decay of maximum amplitude along the transverse direction that was a function of damping for a constant *Re*. Soti et al. (2018) studied experimentally the effect of damping on the VIV response at mass ratio 3 for Reynolds numbers of 1200 to 11 000. Unlike previous studies, they relied on the frequency response for branch identification and argued for the presence of the upper branch for a much larger value of mass-damping then previously reported.

All the aforementioned work was done for a circular cylinder elastically supported by a spring–damper system in parallel. In the spring–damper parallel system (also referred to as the Kelvin-Voigt model Findley and Davis, 2013), the amplitude response decreases with increasing damping due to an increase in the dissipation of the mechanical energy of cylinder by the damper. de Lima et al. (2018) have proposed the use of a 1-DOF viscoelastically-mounted cylinder in fluid flow at Reynolds number 10 000 to suppress the vibrations induced by vortex shedding. Importantly, the frequency and temperature play a significant effect on viscoelastic properties, and were considered in that investigation.

However, recent studies by Mishra et al. (2019) on the Standard Linear Solid model (SLS) of viscoelasticity motivated us to use the two springs and damper system as shown in Fig. 1. They have simulated the fluid–structure interaction (FSI) of a viscoelastic thin plate attached to the lee side of the cylinder for $Re = 100$. The displacement amplitude was found to be a non-monotonic function of structural damping. The SLS spring–damper system behaves similarly to the parallel spring–damper system up-to critical damping ratio (ζ_c). However, on a further increase of damping ratio, the amplitude response does continue to decrease. It will be shown that the higher damping ratio ($\zeta > \zeta_c$) response is similar to that at lower damping ratio ($\zeta > \zeta_c$). The non-monotonic vibration amplitude response with damping ratio is summarized in a "Griffin Plot" presented later in the paper. To the knowledge of the authors, the dynamical behaviour of an SLS

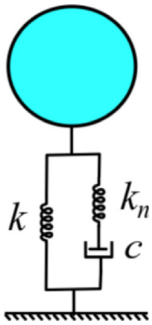

Fig. 1. Schematic of the spring + spring–damper system used in present VIV study.

spring–damper system at low mass ratios has received little or no attention in the literature, yet it provides an effective means of tuning the amplitude response for VIV suppression or energy extraction applications.

The layout of this paper is as follows. In Section 2, the governing equations for the structure (SLS spring–damper system), fluid flow, and coupling of the flow and structural solvers are provided. The numerical approach to solve this coupled system is also briefly discussed. In Section 3, a mathematical model of a simple spring-dashpot model of SLS is presented. This model helps to predict the complex phenomenon of VIV for the SLS system. The simulation results are given in Section 4 as a function of the two governing parameters of the SLS model. These parameters are: (a) damping ratio ζ, and (b) the ratio of spring constants of the two springs (R). The influence of these parameters on the amplitude of the vibration is been discussed. The branching based on the vibration amplitude response and maximum lift force, which leads to the beginning of the upper-type branch at low Re is also discussed.

2. Problem definition and methodology

2.1. Governing equations

In the present work, a circular cylinder of diameter D is placed in a free-stream flow. The cylinder mounted vertically on viscoelastic support, as shown in Fig. 2, is free to oscillate in the transverse direction, perpendicular to flow. The flow is assumed two-dimensional (2D) based on the considered Reynolds number. The fluid is assumed to be incompressible and viscous, while the motion of the cylinder behaves as a spring–mass–damper system as depicted in Fig. 1. Fluid flow is modelled in the moving reference frame attached to the cylinder. The governing equations are the non-dimensional Navier–Stokes equations in an accelerated frame of reference

$$\frac{\partial u_i}{\partial t} + \frac{\partial u_j u_i}{\partial x_j} = -\frac{\partial p}{\partial x_i} + \frac{1}{Re}\frac{\partial^2 u_i}{\partial x_j^2} + a_i, \tag{1}$$

$$\frac{\partial u_i}{\partial x_i} = 0, \tag{2}$$

where u_i and p are the fluid velocity and kinematic pressure, respectively, and a_i is the acceleration of the reference frame attached to the cylinder. The free-stream velocity U_∞ and the cylinder diameter D are used as velocity and length reference scales to non-dimensionalize the system. The motion of the cylinder spring–damper system is derived as follows.

The constitutive equation of the three-element system shown in Fig. 1 is given by

$$F_{int} + \frac{c}{k_n}\frac{dF_{int}}{dt} = ky + c(1 + \frac{k}{k_n})\frac{dy}{dt}. \tag{3}$$

Here, F_{int} is the internal force due to spring–damper system. Combining the constitutive equation with the dynamic equation, $md^2y/dt^2 = F_y - F_{int}$, the differential equation of the motion of the cylinder is

$$\frac{mc}{k_n}\frac{d^3y}{dt^3} + m\frac{d^2y}{dt^2} + c(1 + \frac{k}{k_n})\frac{dy}{dt} + ky = F_y + \frac{c}{k_n}\frac{dF_y}{dt}. \tag{4}$$

Using $\zeta = c/2\sqrt{km}$, $f_n = \frac{1}{2\pi}\sqrt{\frac{k}{m}}$ and $R = k_n/k$, Eq. (4) can be expressed as:

$$\frac{\zeta}{R\pi f_n}\frac{d^3y}{dt^3} + \frac{d^2y}{dt^2} + 4\pi\zeta f_n(1 + \frac{1}{R})\frac{dy}{dt} + 4\pi^2 f_n^2 y = \frac{F_y}{m} + \frac{\zeta}{\pi f_n m R}\frac{dF_y}{dt}. \tag{5}$$

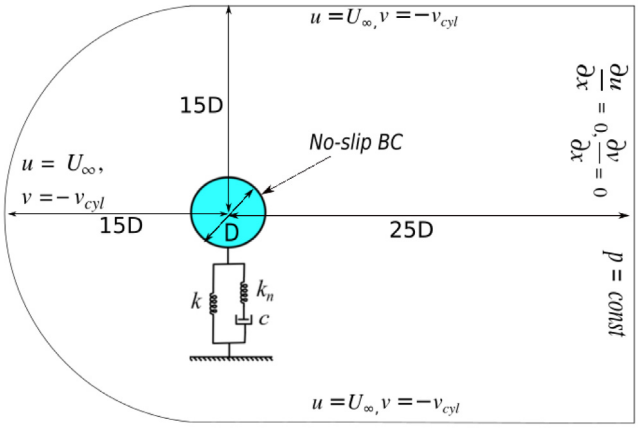

Fig. 2. Schematic of the computational domain and the boundary conditions for the vortex-induced vibration problem.

Next, incorporating non-dimensional variables, $Y^* = y/D, t^* = U_\infty t/D, f_n^* = Df_n/U_\infty, m^* = 4m/\pi\rho D^2$, and $C_L = 2F_y/\rho D U_\infty^2$, the dimensionless structural differential equation reduces to:

$$\dddot{Y}^* + \frac{R\pi f_n^*}{\zeta}\ddot{Y}^* + 4\pi^2 f_n^{*2}(R+1)\dot{Y}^* + \frac{4\pi^3 R f_n^{*3}}{\zeta}Y^* = \frac{2Rf_n^*}{\zeta m^*}C_L + \frac{2}{\pi m^*}\dot{C}_L. \tag{6}$$

Here Y^* and C_L corresponds to the displacement and lift force, respectively. Also, $\dddot{Y}^*, \ddot{Y}^*, \dot{Y}^*$ and Y^* are the non-dimensional jerk, acceleration, velocity and displacement of the cylinder. Additionally, f_n^* is the non-dimensional frequency, where the natural frequency of the system in a vacuum is $f_n = \frac{1}{2\pi}\sqrt{k/m}$, and m^* is mass ratio. The mass ratio is defined as $m^* = 4m/\pi\rho D^2$ where m and ρ are the mass per unit length and the fluid density, respectively.

The coupled fluid–solid system is described by the incompressible Navier–Stokes equations, given by Eqs. (1) and (2), together with the equation of motion for the cylinder expressed by Eq. (6).

2.2. Numerical approach

The simulations employed a non-deformable moving mesh fixed to the cylinder causing an extra non-inertial acceleration term to be added to the right-hand side of the Navier–Stokes equations (refer Eq. (1)) to account for the frame acceleration. A spectral-element technique is employed for the spatial discretization (e.g., see Karniadakis and Sherwin, 2013). The implementation of the spectral-element method is given in Thompson et al. (1996, 2006), hence only a brief description of the approach is given here.

The spatial domain is discretized into quadrilateral elements, which can have curved sides, thus accurately accounting for the cylinder curvature. Within each element, the velocity and pressure fields are represented by high-order tensor-product Lagrangian polynomial shape functions. The node points of these polynomial functions are given by Gauss–Lobatto–Legendre quadrature integration points. The time integration of the spatially discretized equation was dealt with by a three-step time-splitting scheme that sequentially accounts for the advection, pressure and diffusion terms of Navier–Stokes equations. First, the velocity field is updated taking into account advection and cylinder acceleration using an explicit third-order Adams–Bashforth method. Second, the pressure step accounts for the effect of the pressure gradient on the velocity field. This proceeds by taking the divergence of the update step to form a Poisson equation for the pressure forced by the divergence of the velocity field after the advection step. Once the pressure is evaluated (through LU decomposition), the intermediate velocity is updated resulting in a divergence-free field. The final substep corrects the velocity for the effect of diffusion over the timestep. The substep employs the Crank–Nicholson scheme for the update. A detailed implementation of time-splitting scheme can be found in Thompson et al. (2006).

The structure motion is solved by a predictor–corrector iterative method. In the first iteration, the motion is predicted explicitly and then is corrected through several corrector iterations. This is done in a coupled manner with the Navier–Stokes solver. The details of the coupled predictor–corrector Navier–Stokes iterations employed are presented in Leontini et al. (2006a) and Rajamuni et al. (2018).

2.3. Computational domain and boundary conditions

As indicated above, we investigate the VIV of a cylinder at low Reynolds number under *viscoelastic* support. A schematic of the computational domain is shown in Fig. 2. The cylinder is constrained to move in the transverse direction to the

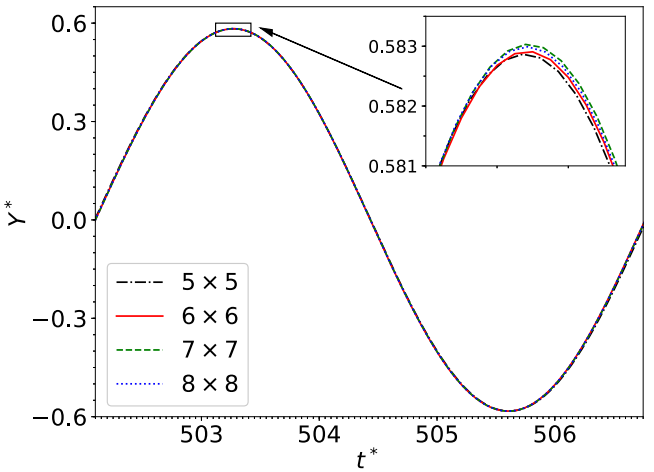

Fig. 3. The resolution study of spectral-element convergence for VIV of a circular cylinder at $Re = 150$, $U_r = 4$, $R = 1$, $\zeta = 0.001$. See text for details.

flow. We explore the following parameter ranges: damping ratio – $\zeta \in [0.001, 10]$; Spring stiffness ratio – $R \in [0, 10]$. The Reynolds number is fixed at $Re = 150$, below the transition to three-dimensional flow even for the stationary cylinder.

The computational domain is shown in Fig. 2. The inlet is semicircular with diameter $30D$ and the far-field extends $25D$ in the downstream direction. This leads to a blockage ratio of approximately 3%. The vibrating cylinder remains at the centre of the semicircle. The mesh consists of 518 spectral elements, concentrated towards the cylinder and in the downstream wake to capture the higher gradients in those regions. The flow boundary conditions are shown in Fig. 2, and are described as follows. The background fluid velocity is prescribed at the inlet, top, and bottom boundaries as $u = U_\infty$ and $v = -v_{cyl}$, with u and v are the x and y velocity components, respectively, and v_{cyl} is the cylinder velocity in the absolute frame. At the surface of the cylinder, the no-slip condition is imposed. The pressure boundary condition is obtained by taking the dot product with the boundary surface normal and the (vector) Navier–Stokes equation, which, upon rearranging, gives an expression for the normal pressure gradient (Karniadakis et al., 1991). This is used to set the pressure boundary condition at both the cylinder and side/inflow boundaries. At the outflow boundary, the pressure is set to a constant and normal component of the velocity gradient is set to zero.

2.4. Resolution studies

All VIV simulations presented in the paper were carried out based on 6×6 nodes per elements for the macro-elements of the mesh. To demonstrate that this resolution is sufficient to resolve the flow in VIV simulations, the temporal variation of the cylinder displacement is shown in Fig. 3. Four sets of element resolutions (5×5, 6×6, 7×7, and 8×8) for a parameter set that leads to near-maximal displacement: $U_r = 4$, $\zeta = 0.001$, $R = 1$. Fig. 3 indicates 6×6 node elements predict the oscillation amplitude to within 0.02% of the high-resolution test cases, providing confidence that the results presented in this paper are adequately converged.

2.5. Code validation

The spectral-element implementation has been previously extensively validated against experiments and other codes, e.g., see Hourigan et al. (2001), Sheard et al. (2003) and Leontini et al. (2006a) and references therein. This solver has also been used to model closely related vortex-induced vibration problems e.g., for a cylinder: Leontini et al. (2006b,a) and Leontini et al. (2011); and a sphere: Lee et al. (2013).

For the present study, we have undertaken further tests of the implementation of the VIV module for a cylinder with a single degree of freedom by considering parameter sets that effectively reduce to the standard elastically mounted cylinder problem. The schematic of the computational domain is shown in Fig. 2, in which the cylinder is mounted on a spring-dashpot viscoelastic model and is free to vibrate only in the transverse direction. To validate against existing elastic results available in the literature, two viscoelastic cases are considered that reduce to simpler elastic cases: (1) $R = 0$; and (2) $\zeta \to \infty$ and $R = 1$, as depicted in Fig. 4. For $R = 0$, the mounting system acts as single spring with frequency f_1, whereas for $\zeta \to \infty$ and $R = 1$, it act as two springs in parallel with an effective system frequency $f_2 = \sqrt{2}f_1$. The response curves for these cases can be compared with previously reported results from the literature.

For these two cases, simulations were performed at $Re = 150$ and $m^* = 2.546$ over a range of reduced velocities. The structural frequencies considered are: case (1) $f_n D/U_\infty = 1/U_r$; and case (2) $f_n D/U_\infty = 1/\sqrt{2}U_r$. The variation of the maximum displacement of the cylinder with reduced velocity is shown in Fig. 5. The comparison shows that our results

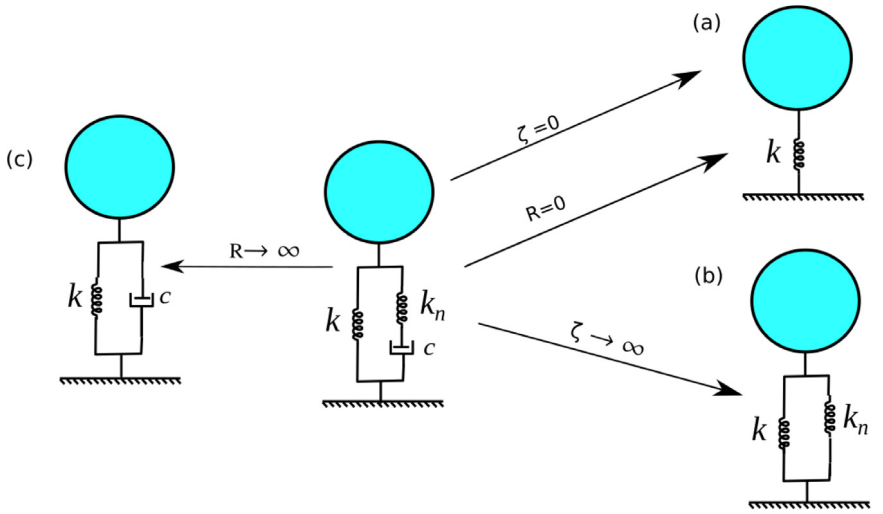

Fig. 4. Schematic of the conversion of the viscoelastic system into an elastic one: (a) $R(=k_n/k)=0$; and (b) $\zeta(=c/2\sqrt{km})\to\infty$, (c) $R\to\infty$. The viscoelastic (Kelvin-Voigt) model is described in Findley and Davis (2013).

agree well with the results of Bao et al. (2012) and Zhao (2013). The minor differences at some reduced velocities may be due to different blockage ratios considered. It should be noted that Bao et al. (2012) quotes a reduced mass of 2 whereas for present simulations it is 2.546. However, this difference is only due to the different definitions of the mass ratio. Bao et al. (2012) takes $m^*=m/\rho_f D^2$, while in the present case $m^*=4m/\pi\rho_f D^2$.

3. A simplified mathematical model of a flexibly mounted cylinder

Experiments of Khalak and Williamson (1999) have shown that in the lock-in region at dynamic steady state, both the displacement and the fluid force have nearly sinusoidal forms and oscillate at the same frequency f_y. In the region where the cylinder oscillation frequency is synchronized with the periodic induced force, the transverse displacement and lift coefficient are given by

$$Y^*=A^*\sin(2\pi f_y^* t^*) \text{ and } C_L=C_{L_0}\sin(2\pi f_y^* t^*+\phi). \tag{7}$$

Here A^* and C_{L_0} represent the non-dimensional amplitude of cylinder and the amplitude of the lift coefficient. Also, f_y^* is the non-dimensional frequency of cylinder oscillation.

The lift force lags the cylinder displacement with a phase difference ϕ. Substituting Eq. (7) in Eq. (6) and comparing the coefficient of $\cos(2\pi f_y^* t)$, we get

$$A^*=\frac{C_{L_0}(2\cos(\phi)\zeta f_y^*+\sin(\phi)Rf_n^*)}{4\pi^3 f_y^*(Rf_n^{*2}-f_y^{*2}+f_n^{*2})\zeta m^*}. \tag{8}$$

Normalizing by natural frequency of the structure, f_s^*, such that $f^*=f_y^*/f_s^*$ and $U_r=1/f_s^*$, we get

$$A^*=\frac{C_{L_0}(2\cos(\phi)\zeta f^* P+\sin(\phi)R)PU_r{}^2}{4\pi^3 f^*(R+1-f^{*2}P^2)\zeta m^*}. \tag{9}$$

Here, $P=f_s^*/f_n^*$, remains constant for a particular ζ. Similarly, comparing the $\sin(2\pi f_y^* t)$ term, and rearranging, we get

$$2A^*\pi^3 R(1-f^{*2}P^2)=\frac{C_{L_0}}{m^*}(RU_r{}^2P^2\cos(\phi)-f^*U_r{}^2P^3 2\sin(\phi)\zeta). \tag{10}$$

The amplitude and frequency expression for limiting case shown in Fig. 4 can be readily derived. For $\zeta=0$ or $R=0$, as shown in Fig. 4(a), the SLS model simplifies to a purely elastic system with spring constant k (say for $P=1$), Eqs. (9) and (10), gives

$$\begin{aligned}\sin(\phi)&=0,\\ \cos(\phi)&=\frac{2A^*\pi^3(1-f^{*2})m^*}{C_{L_0}U_r{}^2}.\end{aligned} \tag{11}$$

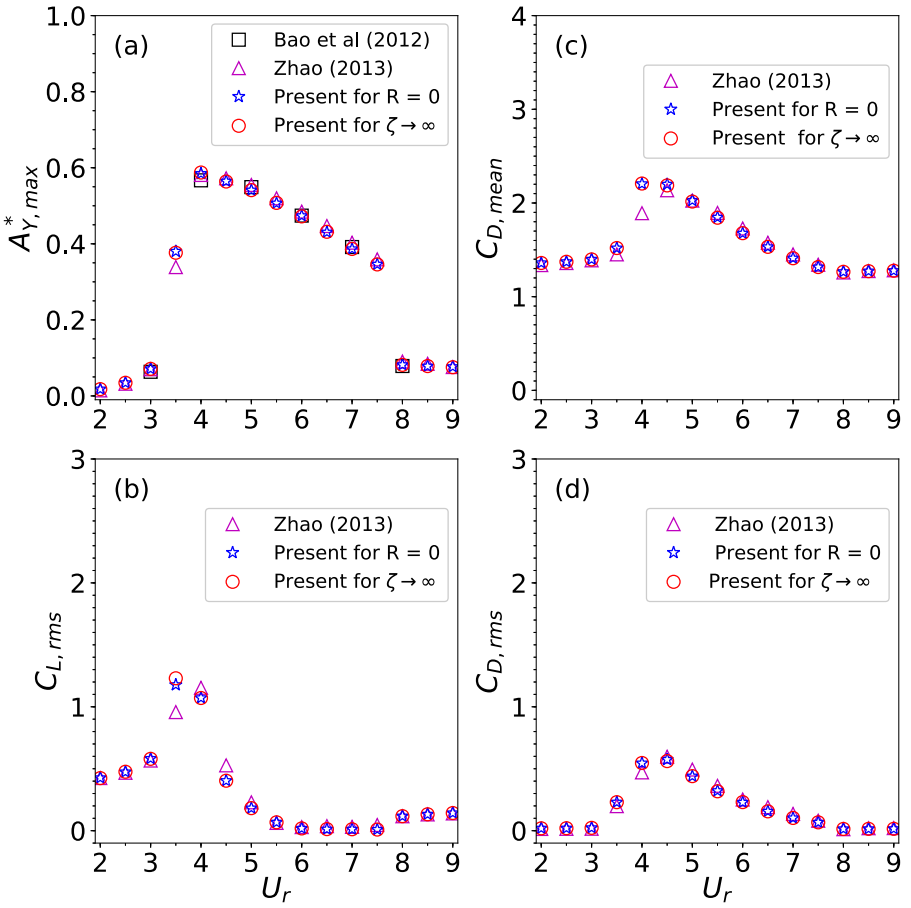

Fig. 5. Comparison of computed maximum displacement amplitude of an undamped cylinder undergoing transverse VIV for $m^* = 2.546$ (Bao et al., 2012; Zhao, 2013) at $Re = 150$.

These are amplitude and frequency equations (Mittal et al., 2017), which clearly shows the phase difference can be 0° or 180°.

For $\zeta \to \infty$, SLS converts into an elastic system with two springs (k, k_n) parallel (Fig. 4(b)). At this limiting case Eqs. (9) and (10) convert into the equations

$$\begin{aligned} \sin(\phi) &= 0, \\ \cos(\phi) &= \frac{2A^*\pi^3(R+1-f^{*2}P^2)m^*}{C_{L_0}{U_r}^2 P}. \end{aligned} \tag{12}$$

For $R \to \infty$, the SLS model becomes the classical spring (k) damper (c) in parallel, as shown in Fig. 4(c). The amplitude and phase equations for this system, assuming $f_n = f_s$, are given by

$$A^* = \frac{C_{L_0}(\sin(\phi)){U_r}^2}{4\pi^3 f^* \zeta m^*}, \tag{13}$$

$$2A^*\pi^3 m^*(1-f^{*2}) = C_{L_0}{U_r}^2\cos(\phi). \tag{14}$$

The response amplitude and frequency expressions are similar to those obtained by Khalak and Williamson (1999).

4. Results and discussion

In this section, the effect of damping (ζ) and spring stiffness ratio (R) on the vortex-induced vibration of a circular cylinder will be discussed. There are five independent parameters in the study: mass ratio (m^*), damping ratio (ζ), spring-stiffness ratio (R), reduced velocity (U_r) and Reynolds number (Re). The reduced velocity is defined as $U_r = U_\infty/(f_s D) = 1/f_s^*$, where U_∞ is the free-stream velocity. Also, f_s and $f_s^*(= f_s D/U_\infty)$, respectively, are the dimensional and non-dimensional natural frequency of the structure considering both the spring and damper. For the present simulations,

Table 1
Reduced velocity U_r, system frequency $f_s^* = f_s D/U_\infty$, and input frequency (f_n^*), for $R = 1$ and $\zeta = 10$.

U_r	f_s^*	f_n^*
2.0	0.5	0.354
3.0	0.333	0.236
4.0	0.250	0.177
5.0	0.200	0.142
6.0	0.167	0.118
7.0	0.143	0.101
8.0	0.125	0.089
9.0	0.111	0.079

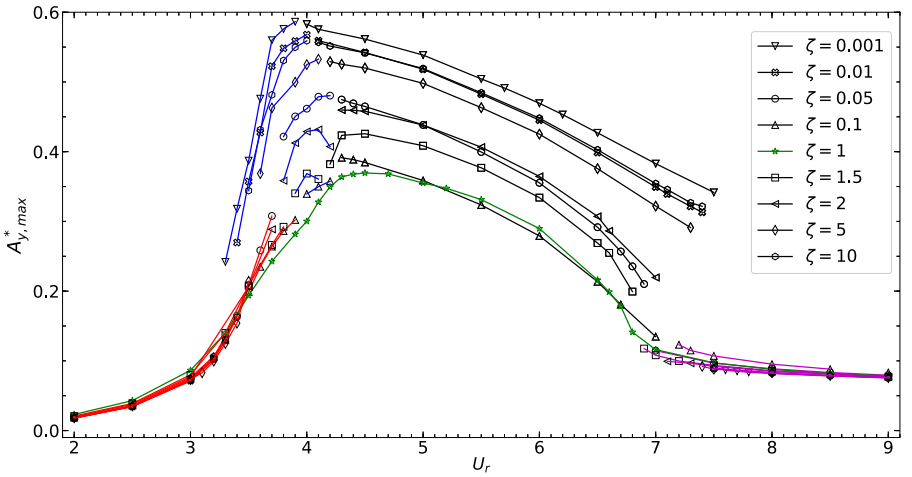

Fig. 6. Response for the cylinder mounted on a viscoelastic support. Variation of amplitude (A^*_{max}) versus reduced velocity (U_r) for damping coefficient in the range $\zeta \in [0.001 - 10]$. The stiffness ratio ($R = 1$) and mass ratio ($m^* = 2.546$) are fixed. (For interpretation of the references to colour in this figure legend, the reader is referred to the web version of this article.)

the reduced velocity was varied by changing f_s while keeping the values of U_∞ and D fixed. The mass ratio is kept at $m^* = 2.546$ to correspond to the simpler VIV system explored in related papers (Bao et al., 2012; Zhao, 2013).

To obtain f_s^*, Eq. (6) with $C_L = 0$ is solved analytically. The solution is of the form

$$y(t) = A_1 e^{-at} cos(bt + \theta) + A_2 e^{-ct}, \tag{15}$$

where A_1, A_2 and θ are constants obtained using initial conditions, b is the angular frequency and $f_s^* = b/2\pi$. The input for Eq. (6) is f_n^* and the reduced velocity is defined using f_s^*. This frequency, f_n^*, is the frequency considering the spring constant k, whereas f_s^* is the natural frequency of the structural system considering k, k_n, ζ. Then f_s^* is used to define the reduced velocity, $U_r = 1/f_s^*$. Therefore Eq. (15) is solved iteratively to get the f_n^*, such that the output is f_s^*. The representative values are given for $R = 1$ and $\zeta = 10$ in Table 1.

4.1. Effect of damping on cylinder response at $R = 1$

The dynamic asymptotic response of cylinder supported by an SLS spring–damper support has been calculated at seven values of damping ratio for $0.001 \leq \zeta \leq 10$, for $R = 1$. This study shows a non-monotonic variation of amplitude with damping ratio, which will be quantified further in the 'Griffin Plot' towards the end of the paper (Section 4.1.4).

4.1.1. Branching behaviour of VIV at low reynolds number

The effect of damping ratio (ζ) on the vibration amplitude ($A^*_{y,max}$) of the circular cylinder is shown in Fig. 6, which shows the amplitude of response ($A^*_{y,max}$) versus reduced velocity (U_r). As observed in low Reynolds number elastically mounted studies discussed above (e.g., Bao et al., 2012; Zhao, 2013), an *apparent* two-branch response can be seen for the reference case ($\zeta = 1$), as shown by the green line. In other viscoelastic cases considered here ($\zeta \neq 1$), there appears to be a more discernible three-branch response, with the blue lines corresponding to an *upper*-type branch, the black lines corresponding to a *lower*-type branch, and the red lines an *initial* branch. The italics here indicate that these branches are not necessarily one-to-one related to those observed for high-Reynolds number VIV at low mass damping ratio. For the lower-type branch, i.e., the black lines in Fig. 6), the values of the vibration amplitude ($A^*_{y,max}$) steadily decrease with

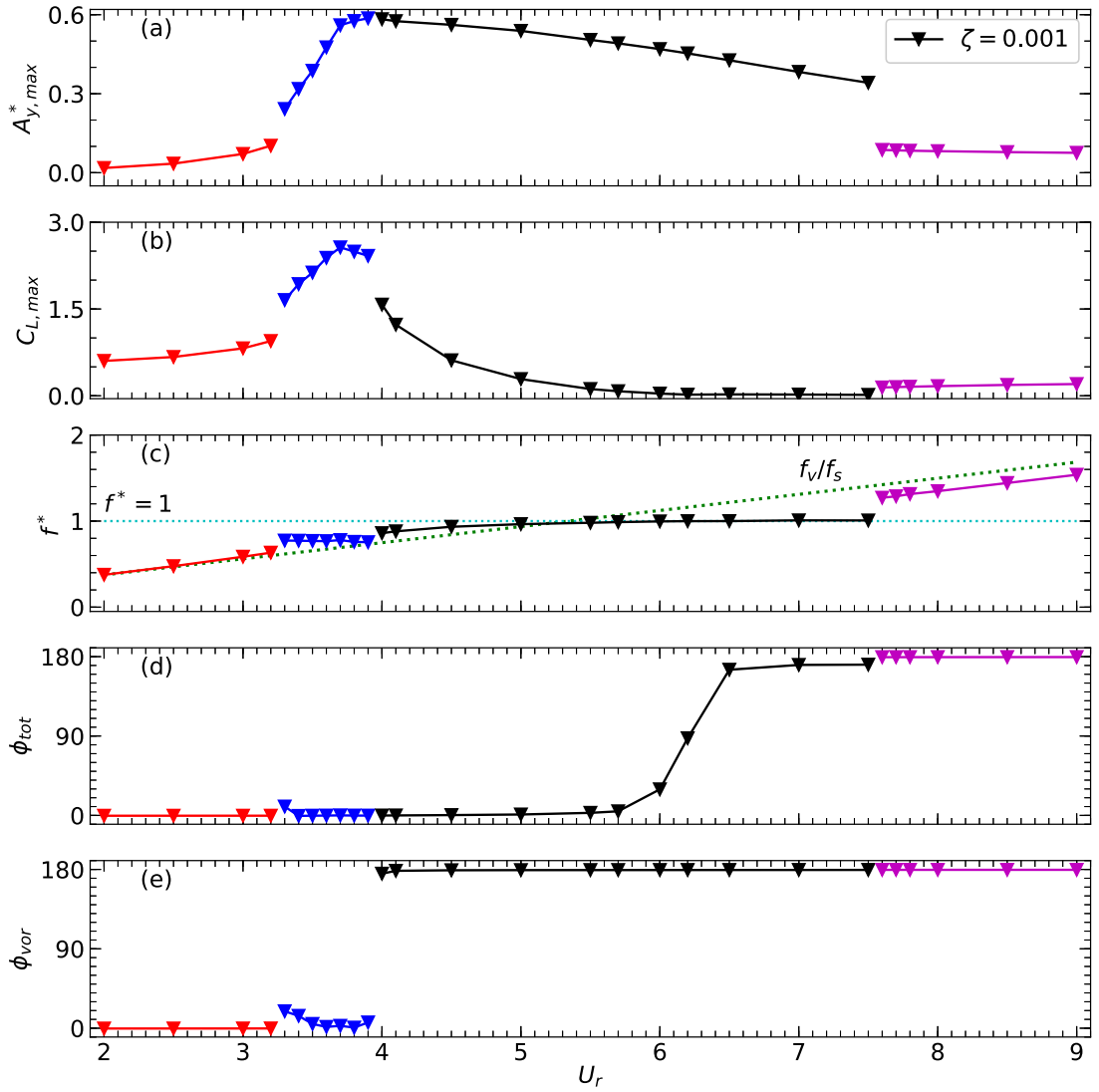

Fig. 7. Response of the cylinder mounted on a viscoelastic support for $\zeta = 0.001$. (a) Maximum oscillation amplitude (A^*_{max}); (b) Peak lift coefficient, $C_{L,max}$; (c) Normalized frequency, $f^* = f^*_y/f^*_s$ (Green dotted line represents the vortex shedding frequency for a stationary cylinder); (d) Mean phase difference between lift force and cylinder displacement, ϕ_{tot}; (e) Mean phase difference between vortex force and cylinder displacement, ϕ_{vor}. (For interpretation of the references to colour in this figure legend, the reader is referred to the web version of this article.)

reduced velocity (U_r). A similar steady decrease in vibration amplitude at *high Re* was observed by Klamo et al. (2006) and Soti et al. (2018) for their highest damped case. In contrast to this steady decrease, Soti et al. (2018) observed a three-branch response from an experimental study, showing that $A^*_{y,max}$ does not vary significantly with U_r over the lower branch for the least damped case.

The detailed response and branching were further examined for the lowest damped case ($\zeta = 0.001$). As evident from Fig. 7(a) the amplitude is a continuous function of U_r, except that there is a sudden jump at $U_r = 3.3$ between the initial and upper-type branches, thus defining the branch ranges as: initial – $2 \leq U_r \leq 3.2$, upper-type – $3.3 \leq u_r \leq 3.9$, and lower-type – $4.0 \leq U_r \leq 7.5$. The desynchronization region is visible over the reduced velocity range: $U_r > 7.6$. Although the amplitude varies continuously (or nearly continuously) over $3.3 \leq U_r \leq 7.5$, Fig. 7(b) shows there is a sudden jump in the amplitude of the lift force (shown by the blue line), thus allowing the identification of a branch transition from the upper to lower branch at $U_r \simeq 4.0$. Indeed, this jump in peak lift force was also observed by Leontini et al. (2006b) for the standard transverse low Reynolds number VIV case.

Interestingly there are also branch-to-branch jumps in the oscillation frequency, represented in terms of normalized frequency. The variation of normalized frequency ($f^* = f^*_y/f^*_s$) for lowest damping, $\zeta = 0.001$, is shown in Fig. 7(c), where f^*_y is the frequency corresponding to the highest power in the power-spectral density (PSD) plot of displacement, and f^*_s is the natural frequency of the system, calculated using Eq. (6). In the region $2 \leq U_r \leq 3.2$, the vibration frequency

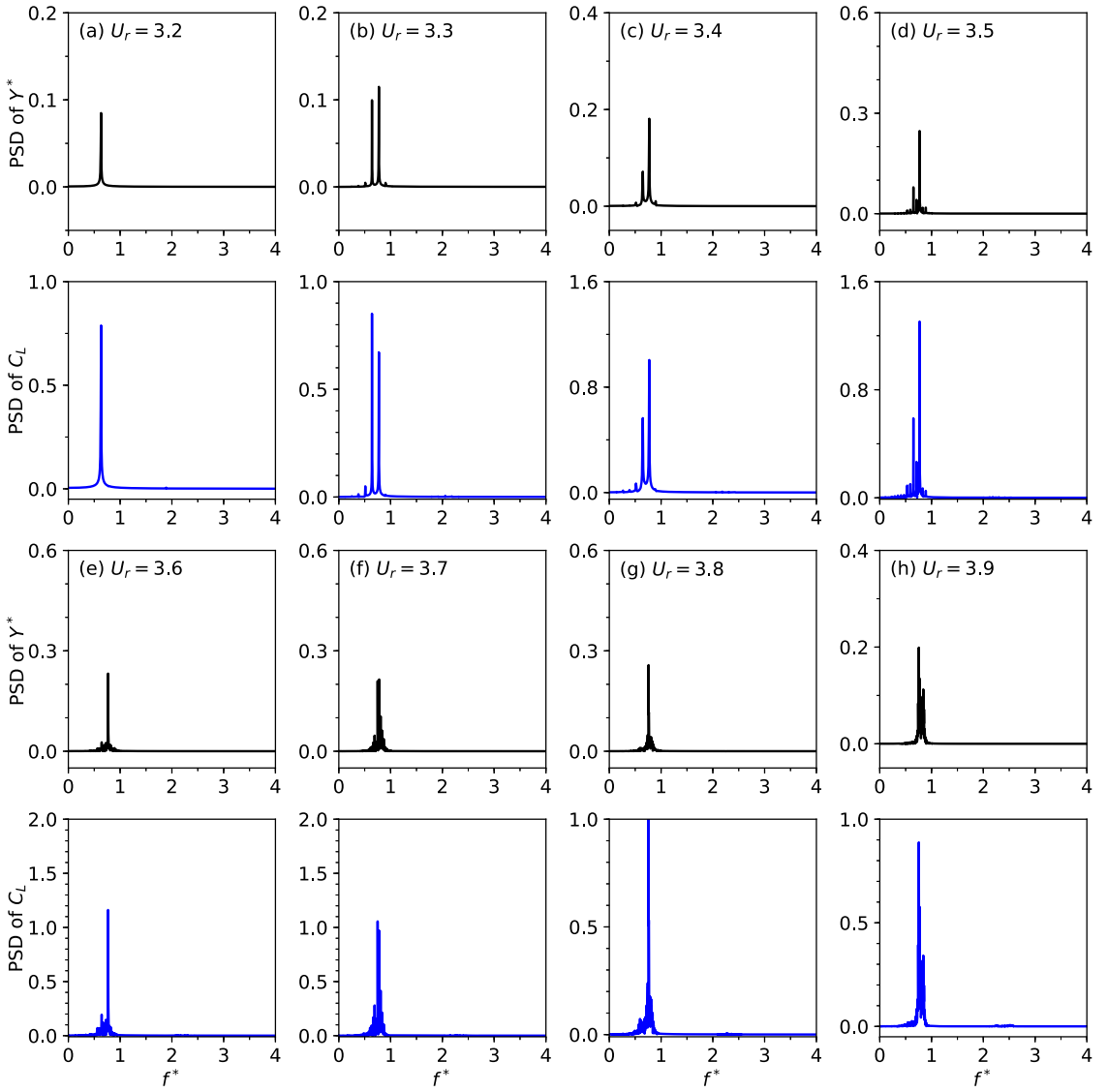

Fig. 8. Power spectral density (PSD) of the cylinder response for displacement (black colour) and lift force (blue colour): (a) $U_r = 3.2$; (b) $U_r = 3.3$; (c) $U_r = 3.4$; (d) $U_r = 3.5$; (e) $U_r = 3.6$; (f) $U_r = 3.7$; (g) $U_r = 3.8$; (h) $U_r = 3.9$. (For interpretation of the references to colour in this figure legend, the reader is referred to the web version of this article.)

(f_y/f_s) overlaps with the vortex-shedding frequency associated with a stationary cylinder ($f_v^* = f_v/f_s$) (represented by the green dotted line in Fig. 7(c)). The vortex-shedding frequency for a stationary cylinder is calculated by computing the FFT of lift force of the stationary cylinder. In this (initial branch) range, the PSD plot of displacement (Y^*) and lift force (C_L) signal, Fig. 8(a), shows that a single frequency is present in Y^* and C_L, which is close to the vortex-shedding frequency for a stationary cylinder, f_v^*. The upper branch shows the dominant oscillation frequency matches the system frequency, whilst for the lower branch, the oscillation frequency approximately matches the natural shedding frequency (dotted green line). However, in the (upper branch) range $3.3 \leq U_r \leq 3.9$, multiple frequencies are present as shown in Fig. 8(b,h). The Lissajous figures (phase plots of C_L versus Y^*), as shown in Fig. 10(b,h), suggest that the time signals of C_L and Y^* are associated with multiple frequencies. Fig. 10 indicate the periodic nature of the oscillations in the lower branch (Fig. 10(i,o)), and the relatively less steady dynamics of the upper branch (Fig. 10(b, h)). The Fig. 10 also suggests the phase changes from 0° (Fig. 10(a, m)) to 180° (Fig. 10(n, p)).

The peak frequency over $3.4 \leq U_r \leq 3.9$ is lower than that at $U_r > 4$, as shown in Fig. 7(c). Over the range $3.9 \leq U_r \leq 7.5$ – the high-amplitude region – the vibration frequency moves away from the shedding frequency of the fixed cylinder and approaches the natural frequency of the system (as $f^* \longrightarrow 1$). In this region (Fig. 9(d)), one component of frequency is present in the displacement signal that corresponds to the vortex-shedding frequency for a stationary

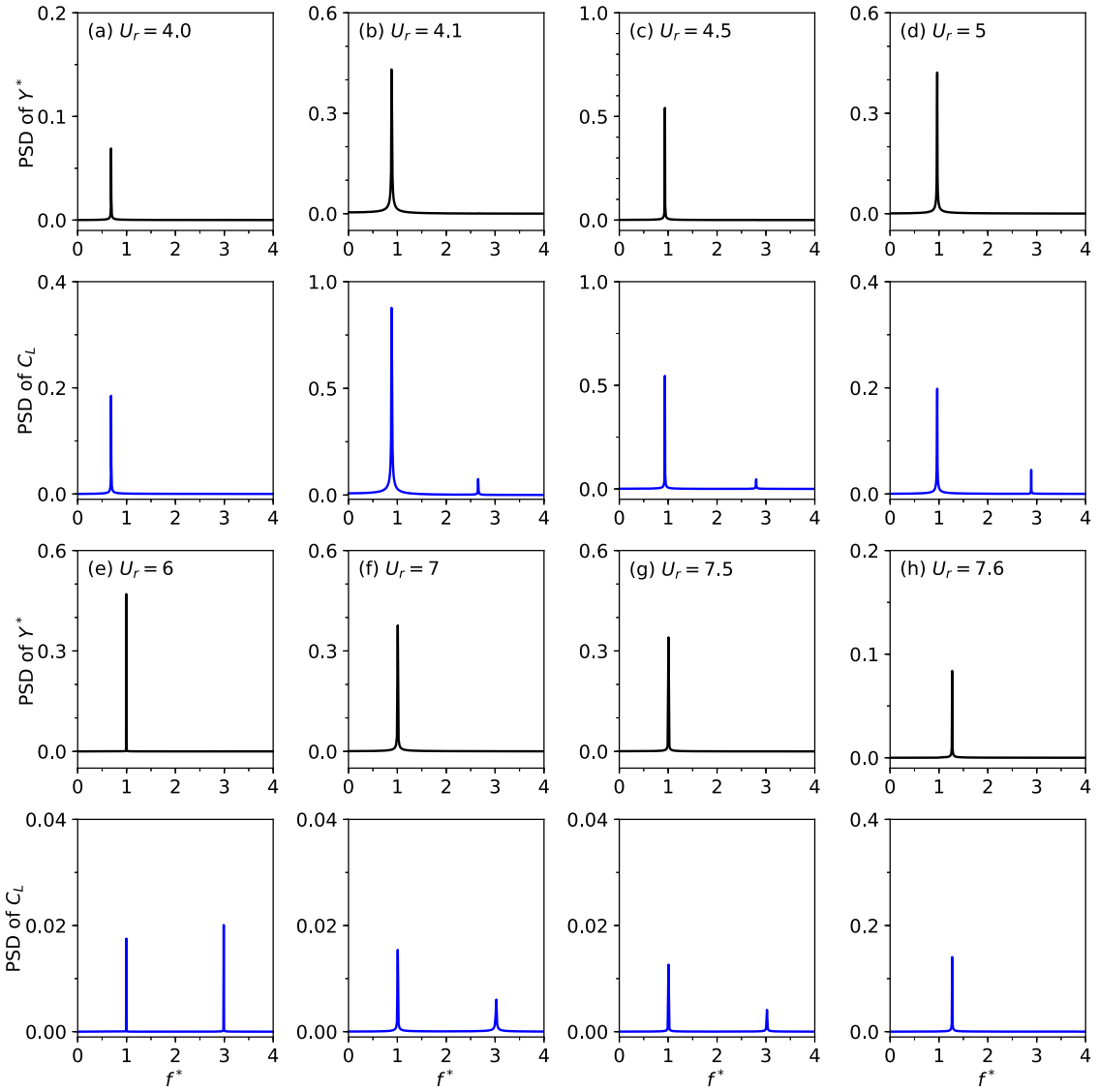

Fig. 9. Power spectral density (PSD) of the cylinder response for displacement (black colour) and lift force (blue colour): (a) $U_r = 3.2$; (b) $U_r = 3.3$; (c) $U_r = 3.9$; (d) $U_r = 4$; (e) $U_r = 6$; (f) $U_r = 7$; (g) $U_r = 7.5$; (h) $U_r = 7.6$. (For interpretation of the references to colour in this figure legend, the reader is referred to the web version of this article.)

cylinder. In the PSD of C_L, two prominent peaks are visible in the lift forces Fig. 9 (e,f,g). The first peak corresponds to vortex shedding and becomes more dominant with an increase of U_r and other is due to the natural frequency of the system. In the desynchronization region, ($U_r \geq 7.6$), only one frequency is present that is closer to f_v^*.

This high amplitude region, ($3.3 \leq U_r \leq 7.5$), shows two behaviours based on peak lift force and frequency, with a weak transition between the two occurring at approximately $U_r \approx 4$. This branching has been previously reported by Leontini et al. (2006b) for a low mass-damping parameter ($m^*\zeta = 0.1$) for $Re = 200$. The regime $3.3 \leq U_r < 4$ coincides with an upper-type response and the synchronized regime $4 \leq U_r \leq 7.5$ coincides with a lower-type branch, consistent with the low Reynolds number characterization of Leontini et al. (2006b). This (beginning of an) upper-type branch response is also evident in the phase difference plot Fig. 7(d), which shows that the difference between the lift force and the cylinder displacement is zero in the initial and upper-type branches. The phase between the lift force and displacement in Fig. 7(d) shows a gradual change: from 0° to 180° for $3.3 \leq U_r \leq 7.5$. This gradual change become less steep for $\zeta = 1$ as shown in Fig. 17. This gradual change in phase difference was observed by Leontini et al. (2006b). As previously indicated, at high Reynolds numbers, Khalak and Williamson (1999) have experimentally observed two distinct synchronous branches: the upper and lower branches. The upper branch was characterized as having a vibration frequency close to vortex-shedding frequency, with the phase difference between the lift force and the cylinder displacement of

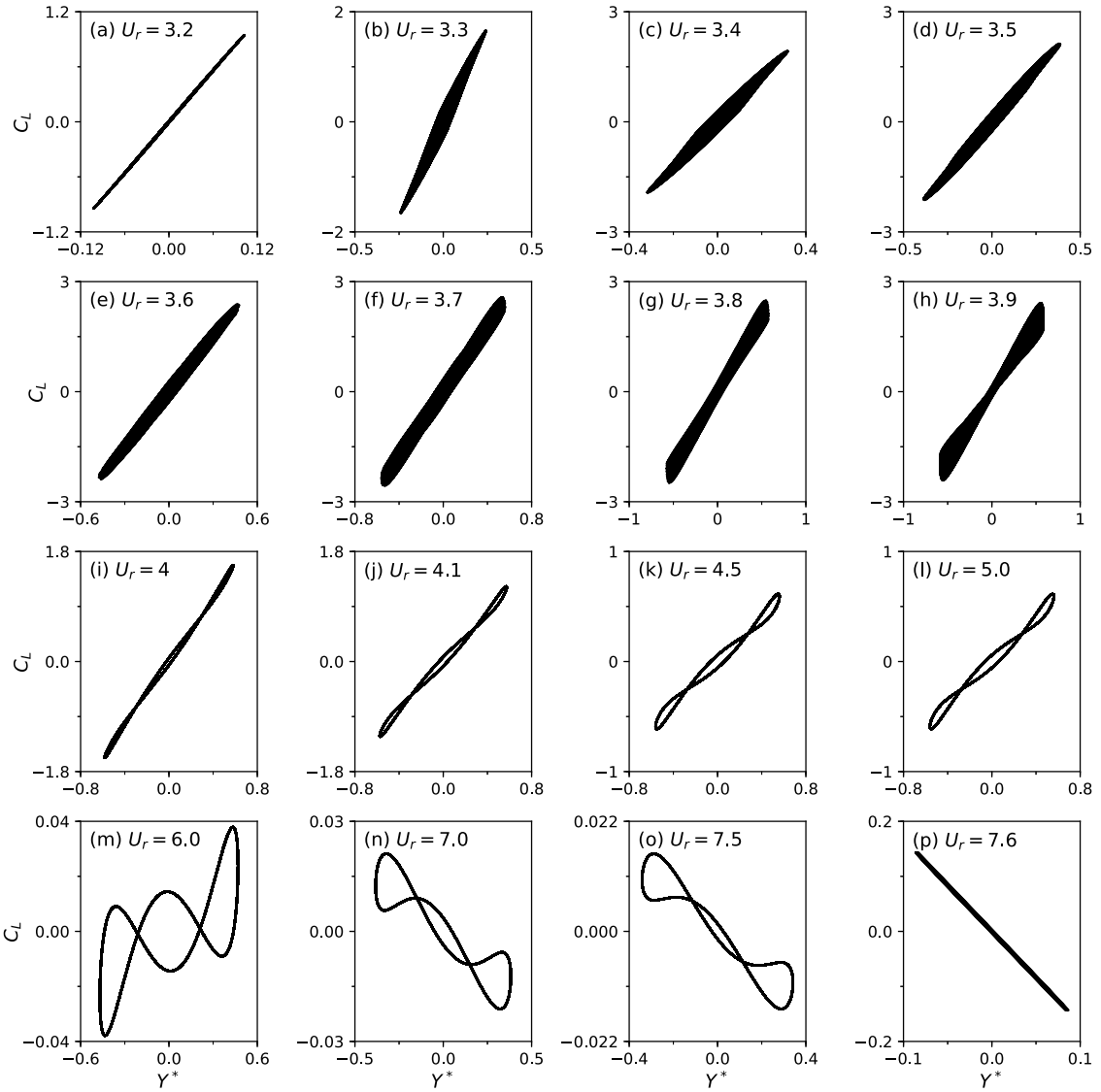

Fig. 10. Lissajous figures of the cylinder response for C_L (along y-axis) and Y^* (along x-axis): (a) $U_r = 3.2$; (b) $U_r = 3.3$; (c) $U_r = 3.4$; (d) $U_r = 3.5$; (e) $U_r = 3.6$; (f) $U_r = 3.7$; (g) $U_r = 3.8$; (h) $U_r = 3.9$; (i) $U_r = 4.0$; (j) $U_r = 4.1$; (k) $U_r = 4.5$; (l) $U_r = 5.0$; (m) $U_r = 6.0$; (n) $U_r = 7.0$; (o) $U_r = 7.5$; (p) $U_r = 7.6$.

zero. The lower branch was characterized as having the vibration frequency close to the natural frequency of the cylinder system, and the phase difference close to 180°. Fig. 7(d) shows the change of phase difference is gradual along the lower branch contrary to the 180° difference observed by Khalak and Williamson (1999) over the entire range. This difference in phasing is presumably due to the low Reynolds number investigated. Fig. 7(e) shows the plot for mean phase difference between vortex-force and cylinder displacement, ϕ_{vor} vs U_r. The calculation of vortex-force and the corresponding phase difference has been discussed in Section 4.1.3. In addition to the jump in the total phase between the upper and lower branches, there is a jump in the vortex phase at the initial to upper branch transition, Fig. 7(e) shows this jump at $U_r = 3.3$ in the vortex phase (ϕ_{vor}). The vortex phase (ϕ_{vor}) is the phase difference between displacement and vortex force (total force − potential added-mass force). The detailed evaluation of the vortex force and the vortex phase is explained in the subsequent section (Section 4.1.3). This jump in the vortex phase was observed in high Reynolds number experiments of Govardhan and Williamson (2000) at the initial to upper branch transition. Overall, based on the jump in peak lift, ϕ_{vor} and the broader response spectrum, the region $3.3 \leq U_r \leq 3.9$ has been designated as an upper-type branch (Leontini et al., 2006b). The vorticity shedding patterns for initial branch ($U_r = 3$) and lower type branch ($U_r = 4.5$) are shown in Fig. 11. In both cases, a 2S vortex shedding mode is observed. In the initial branch, it is a single-row configuration, whereas in the lower-type branch it is a double-row configuration.

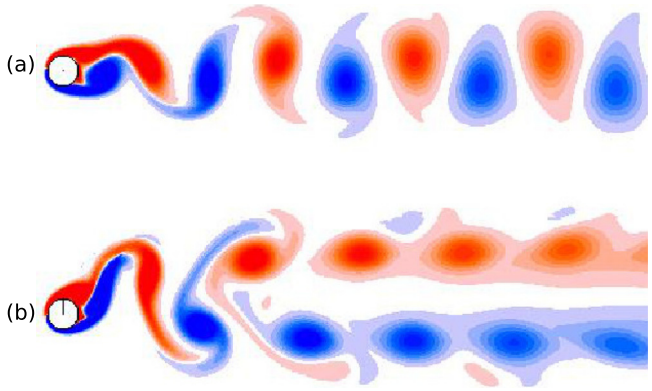

Fig. 11. The cylinder wake depicted by vorticity contours (scale −2 to 2), representative of: (a) the initial branch, $U_r = 3$; (b) the lower-type branch, $U_r = 4.5$; The damping coefficient $\zeta = 0.001$.

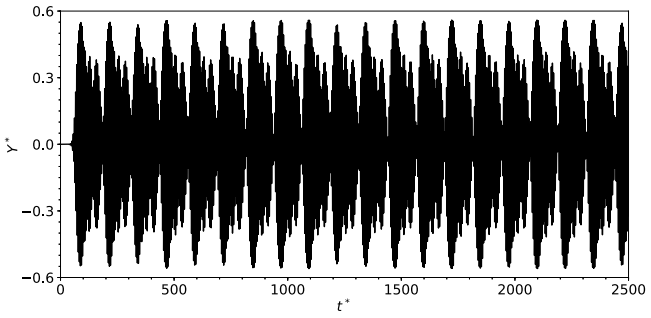

Fig. 12. The amplitude response signal for $U_r = 3.7, \zeta = 0.001$.

The amplitude response signal for $U_r = 3.7$ is shown in Fig. 12, and the corresponding wake patterns for $U_r = 3.7$ corresponding to different periods are shown in Fig. 13. When the amplitude of oscillation is small, the 2S mode of vortex shedding is observed with vortices shed in a single row, whereas a double-row configuration is observed when the amplitude is high. The frequency responses for the displacement and lift are depicted in Fig. 14, which clearly shows *noisy* frequency spectra. Hereafter, we refer to this region as the upper-type branch.

The cylinder response may exhibit hysteresis due to a delay in mode switching during a transition. Hysteresis is caused by the nonlinearity of the system, flow or structural components. Since the structural component is taken as a linear oscillator, hysteresis originates from the fluid system. As shown in Fig. 15, the present simulation results do display hysteretic behaviour, which may further help to demarcate the branches (Khalak and Williamson, 1997). Brika and Laneville (1993) have observed that the cylinder response is sensitive to changing the reduced velocity in small increments, ΔU_r. As reduced velocity is defined as the inverse of the oscillator natural frequency, computations of hysteresis have been carried out with decrements of structural natural frequency, Δf_n^*. For the increasing-velocity curve, the reduced velocity is increased from $U_r = 2$ in small increments with the initial condition at each U_r being the saturated response before the increment. The reduced velocity is increased by decreasing non-dimensional structural natural frequency, f_n^* with decrements size taken is $\Delta f_n^* = 0.001$. For the decreasing velocity-curve, the reduced velocity is decreased from $U_r = 9$ by increasing f_n^*, with the initial condition again corresponding to the fully saturated state for the next level of U_r. A very small hysteretic loop is observed at the onset of the upper-type branch in the range $3.2 \leq U_r \leq 3.3$. Hysteresis for the transition between the lower branch and desynchronization regime is shown in Fig. 15, for a wider range of reduced velocity $7.35 \leq U_r \leq 8.58$. The distinct behaviour in the upper-type branch ($3.33 \leq U_r \leq 3.94$) is further reinforced by the quasi-periodic response, illustrated by the phase-plane plots in Fig. 16.

Next consider the response for the critical damped case ($\zeta = 1$). Fig. 17 shows the variation of amplitude with reduced velocity is continuous without any sign of distinct jumps. As shown in Fig. 17(c), beyond $U_r \geq 6.6$, f^* deviates towards f_v^*, clearly showing the start of desynchronization. The upper-type branch has disappeared. There is no demarcation based on jumps in amplitude, frequency or peak lift force for the initial and lower-type branches. The phase difference Fig. 17(d,e) shows there is a continuous increase of phase as U_r is increased.

For the lower ($\zeta = 0.001, 0.01, 0.05$) and much high damping values ($\zeta = 5, 10$), although the variation of vibration amplitude is continuous (Fig. 6), there is a sudden jump in the amplitude of the lift force (represented by blue lines in Fig. 18). The jump in lift amplitude at the initial to upper branch transition is lost at $\zeta = 0.1, 1, 1.5, 2$. The transition

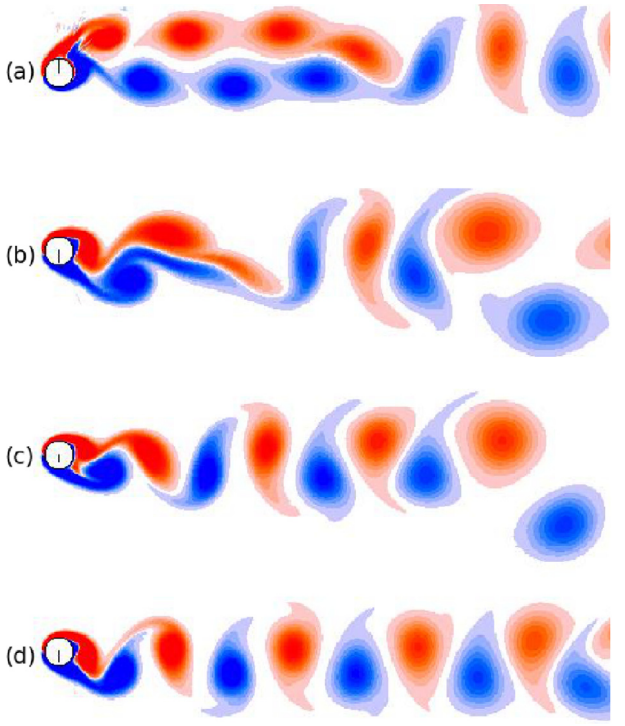

Fig. 13. The wake evolution for $U_r = 3.7$ and $\zeta = 0.001$, representative the variation in the wake observed for the upper-type branch. (a) Double row 2*S* mode; (b) Disordered wake; (c) Wake organizes to single-row configuration; (d) Single-row 2*S* mode.

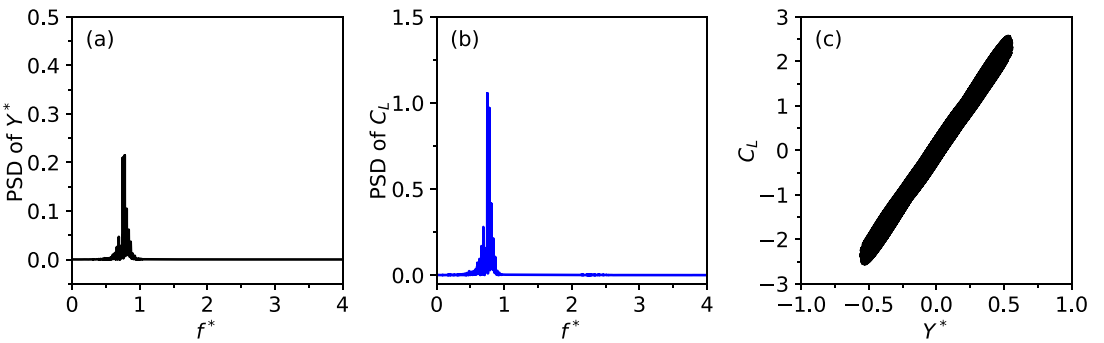

Fig. 14. Power spectral density (PSD) of the cylinder response for (a) Displacement; (b) Lift; (c) Lissajous figure for $U_r = 3.7, \zeta = 0.001$.

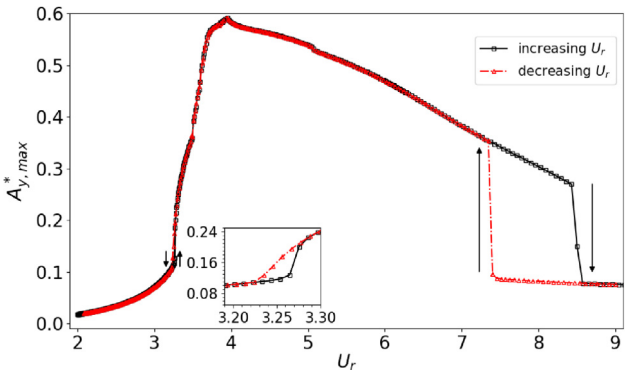

Fig. 15. Response for the cylinder mounted on a viscoelastic support. Variation of amplitude (A^*_{max}) versus reduced velocity (U_r) for $\zeta = 0.001, R = 1$ using increasing and decreasing U_r.

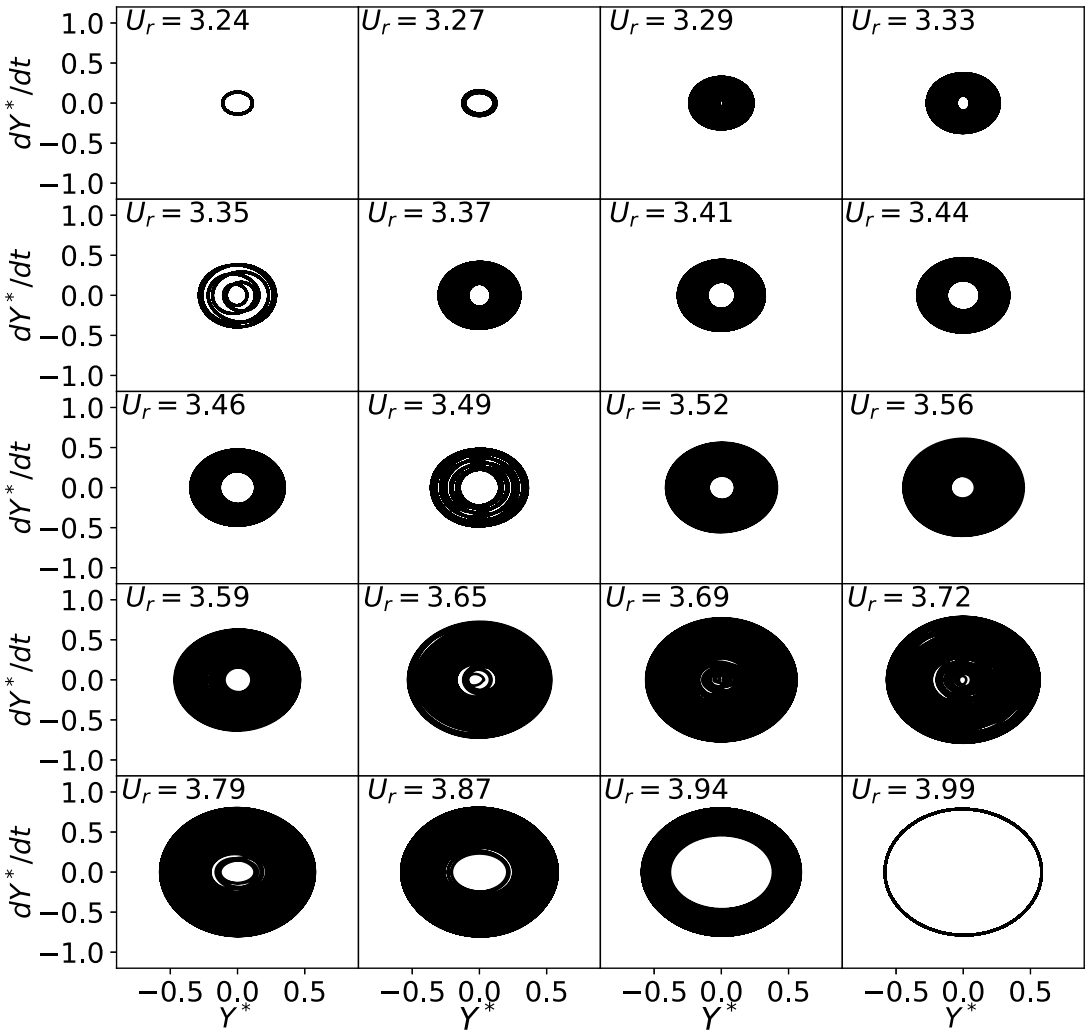

Fig. 16. Phase-plane plots to depict the quasi-periodic behaviour close to the onset of the upper branch, $3.24 \leq U_r \leq 3.29$, and the upper-type branch, $3.33 \leq U_r \leq 3.94$.

between branches becomes continuous, clearly indicates missing upper branch for $\zeta = 0.1, 1, 1.5, 2$. This indicates there is a change in the very character of the flow as damping is increased. The variation of the amplitude of the lift force together with the normalized frequency and phase difference will be used to demarcate the upper-type branch.

4.1.2. Vibration amplitude and the frequency response

The vibration amplitude in Fig. 6 is seen to decrease with an increase in the damping ratio for any reduced velocity until reaches the critical damping ratio. On a further increase of damping, the amplitude increases. It is interesting to note that above or below the critical damping value ($\zeta = 1$), the vibration response is similar. This (*seemingly*) anomalous behaviour has been shown for $\zeta = 0.01$ and $\zeta = 10$ in Fig. 19. This non-monotonic behaviour of amplitude with structural damping occurs due to the SLS type of viscoelastic support considered. This characteristic is expected as the structural model considered behaves purely elastically without damping at the extreme values of damping. As shown in Fig. 4, at $\zeta = 0$, the SLS model acts as a single spring system, whereas for $\zeta \to \infty$ it acts as a two-spring system without damping.

It is evident from Fig. 18 that the jump from the initial to the upper-type branch is delayed as the damping coefficient is increased. It occurs at $U_r = 3.3$ for $\zeta = 0.001$, whereas at $U_r = 3.8$ for $\zeta = 0.05$; beyond this it is not possible to distinguish a jump. We also observe that as damping is increased up to the critical value ($\zeta = 1$), the value of U_r corresponding to the system entering the desynchronized region (pink lines) decreases. For $\zeta = 0.001$, desynchronization starts from $U_r = 7.6$, whereas for $\zeta = 0.05$, it starts from $U_r = 7.0$. The early start of desynchronization can be justified by the normalized frequency plot Fig. 20, which shows an early departure from the $f^* = 1$ line on increasing the damping. As Fig. 20(a) shows, the departure for desynchronization is shifted towards the left from $\zeta = 0.001$ (black line) to $\zeta = 0.1$

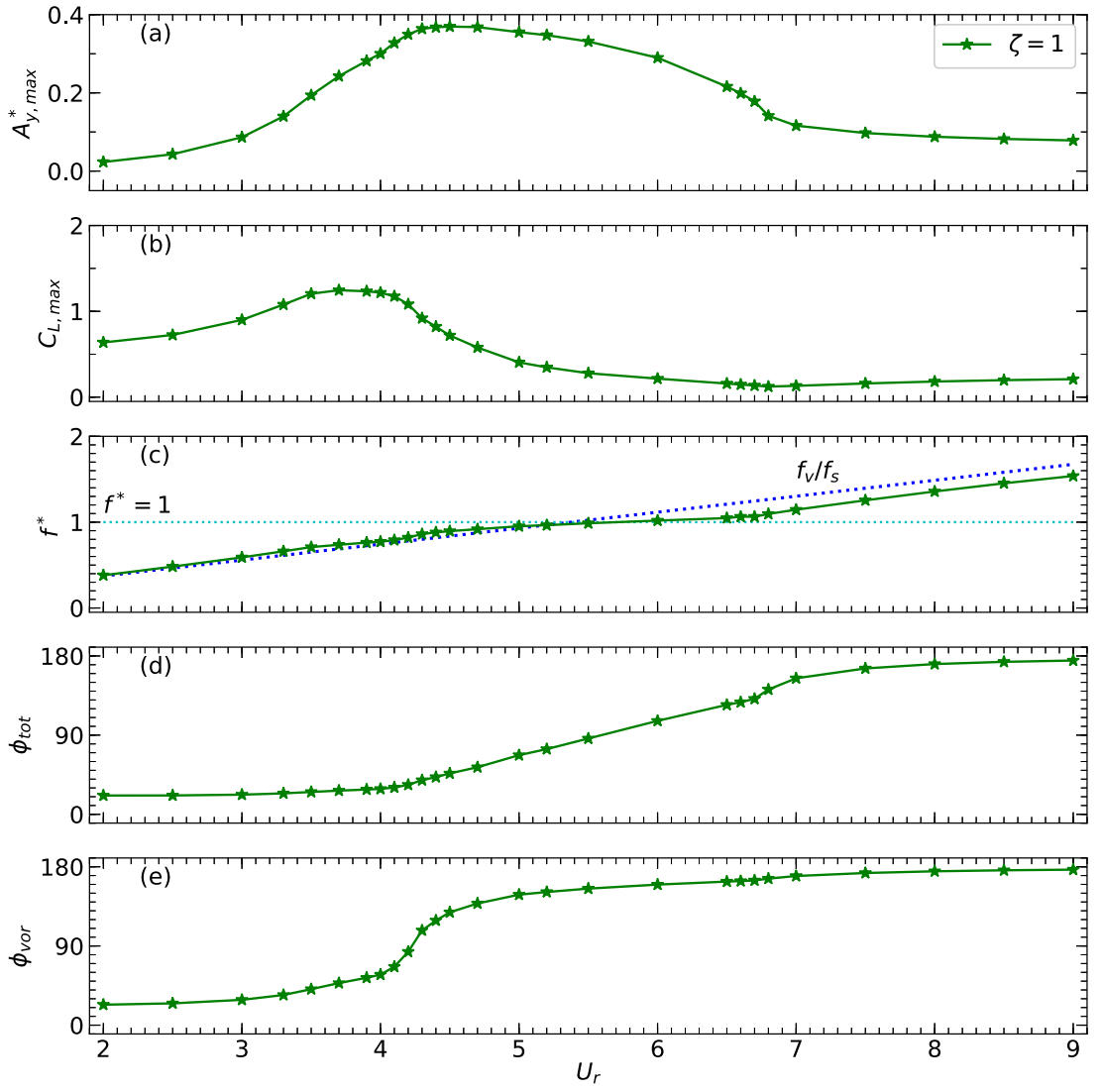

Fig. 17. (a) Amplitude; (b) Peak lift coefficient; (c) Normalized frequency (Blue line represents vortex shedding frequency for stationary cylinder); (d) Mean phase difference between lift and displacement; (e) Mean phase difference between vortex and displacement. All variables are plotted against reduced velocity for $\zeta = 1$ – the critically damped case. (For interpretation of the references to colour in this figure legend, the reader is referred to the web version of this article.)

(purple line). The monotonic decrease in the desynchronized region with damping has been reported by Klamo et al. (2006). The end of the initial branch is shifted towards the right as the damping ratio is increased, as evident from Fig. 20(a). The delay in the initial branch and early start of the lower-type branch with damping ratio, narrows the lock-in region. This trend is reversed on further increasing the damping beyond $\zeta = 1$ as shown in Fig. 20(b). For $\zeta = 1.5$, desynchronization starts from $U_r = 6.9$, while for $\zeta = 10$, it starts from $U_r = 7.5$. The lock-in region broadens with the increase of damping ratio. The non-monotonic trend observed in our results is due to the structural system (SLS) considered. As discussed, it can be observed that if $\zeta = \infty$, the SLS model of spring–damper system represents two springs (Fig. 4(b)) in parallel, where again the vibration is purely elastic. Again, for $\zeta = 0$, the SLS model behaves as the vibration of a single spring (Fig. 4(a)).

4.1.3. Force coefficient and phase difference

The root-mean-square (RMS) lift coefficient ($C_{L,rms}$) as function of reduced velocity is plotted in Fig. 21 for different damping ratios. Fig. 21(a) depicts, below the critical damping ratio ($\zeta = 1$), the peak value of $C_{L,rms}$ decreases with an increase in damping, but plateaus near $\zeta = 1$. For a low damping ratio, $C_{L,rms}$ shows a rapid increase with U_r in the initial branch. In the upper-type branch, $C_{L,rms}$ attains a peak value in the beginning then after a slight decrease, it

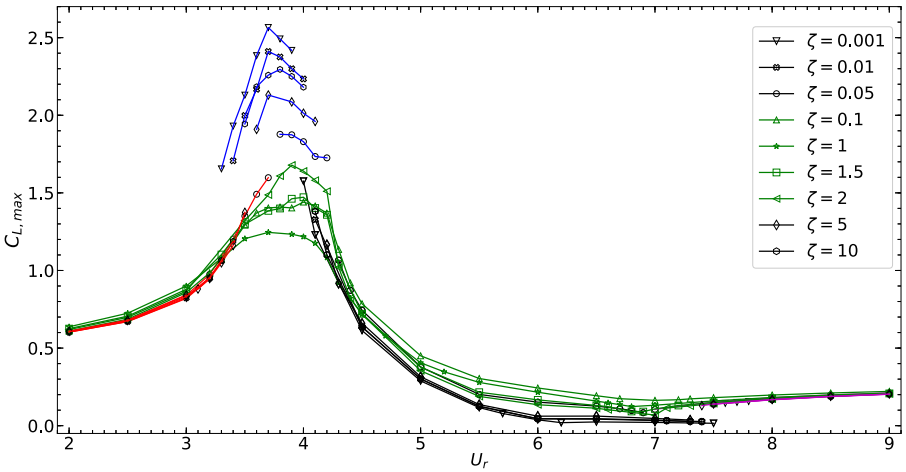

Fig. 18. Variation of maximum lift ($C_{L,max}$) versus reduced velocity (U_r) for damping coefficients $\zeta \in [0.001, 10]$. (For interpretation of the references to colour in this figure legend, the reader is referred to the web version of this article.)

again increases. At the end of the upper-type branch, there is a sudden decrease in $C_{L,rms}$. In the lower-type branch $C_{L,rms}$ decreases exponentially. Finally, in the desynchronization region, it remains constant. For higher damping ratios (i.e. near to $\zeta = 1$), as only the initial and lower-type branches exist, in between there is a negligible change in $C_{L,rms}$ with U_r, presumably because of the missing upper-type branch. For damping ratios where it exists, the upper-type branch shows a drastic variation of $C_{L,rms}$ with U_r. The trend of curves for $\zeta = 0.001, 0.01, 0.05, 0.1$ (Fig. 21(a)) in ascending order is similar to that for $\zeta = 10, 5, 2, 1.5$ (Fig. 21(b)) in descending order. This clearly shows the phenomenon is reversed for damping ratio, $\zeta > 1$.

As discussed by Williamson and Govardhan (2004), the total lift force in the y-direction, F_y can be split into a potential-force component, F_{pot}, and a vortex-force component, F_{vot}. F_{pot} is due to the added mass effect, whereas F_{vot} occur due to vorticity in the flow system. The vortex force can be calculated by

$$F_{vor} = F_y - F_{pot}. \tag{16}$$

Here, F_y is the total lift force, $F_{pot} = -m_a\ddot{y}(t)$, m_a is the added mass due to acceleration of fluid surrounding the body, calculated by considering the hydrodynamic force acting on it as it accelerates from potential flow theory. For a circular cylinder $m_a = \frac{\pi}{4}\rho D^2 L$, where D and L are the diameter and length of the cylinder. Substituting the expression for forces in Eq. (16) and normalizing them by $0.5\rho U_\infty^2 DL$, we get the standard result

$$C_{vor} = C_L - C_{pot}. \tag{17}$$

In this equation, $C_L = F_y/(0.5\rho U_\infty^2 DL)$ is the lift coefficient, C_{vor} is vortex-force coefficient, calculated using Eq. (17).

The RMS vortex-force coefficient, $C_{vor,rms}$ is shown in Fig. 22 for different damping ratio values. It shows $C_{vor,rms}$ increases with U_r in the initial branch up to the start of upper-type branch. It then decreases in the middle of upper-type region. At the end of the upper-type branch range, $C_{vor,rms}$ further decreases to a minimum at the start of the lower-type branch. Towards the end of the upper-type branch, $C_{vor,rms}$ decreases at a faster rate than $C_{L,rms}$ due to higher acceleration resulting in higher potential force. At the beginning of the lower-type branch, $C_{vor,rms}$ increases. On further increase in U_r, $C_{vor,rms}$ drops linearly.

An important quantity to the physics describing vortex-induced vibration is the phase difference between fluid forces and cylinder displacement, obtained using a Hilbert transform (as described by Khalak and Williamson (1999)). The calculated phase difference between the lift force and cylinder displacement is shown in Fig. 23. For very low damping (Fig. 23(a)) and very high damping (Fig. 23(b)), the total phase remains at 0° during the initial and upper-type branch, whereas the total phase switches to 180° on transition to the lower branch. This is evident from Eq. (11) by neglecting the damping, ϕ is limited to be 0° or 180°. The value depends of the sign of $\cos(\phi)$, which shows that $\phi = 0$ for $f^* < 1$ and $\phi = 180$ for $f^* > 1$. A similar argument can be made for very high damping by using Eq. (12). Now for $\zeta = 1$, as shown in Fig. 23, the phase is not restricted to 0° or 180° as can be seen from Eq. (10), because both $\sin(\phi)$ and $\cos(\phi)$ exist. The vortex phase, for very low and very high damping, shows a jump (black line in Fig. 24) at the start of the upper-type branch. The jump is not visible for ζ near to 1, where the upper-type branch disappears. The phase difference moves away from 0° on increasing the damping ratio towards $\zeta = 1$, and on further increasing ζ beyond $\zeta = 1$, ϕ again moves towards 0°. A similar effect is seen in the initial-type branch and desynchronization regime for $\phi = 180°$. The trends can be understood mathematically by manipulation of Eq. (10).

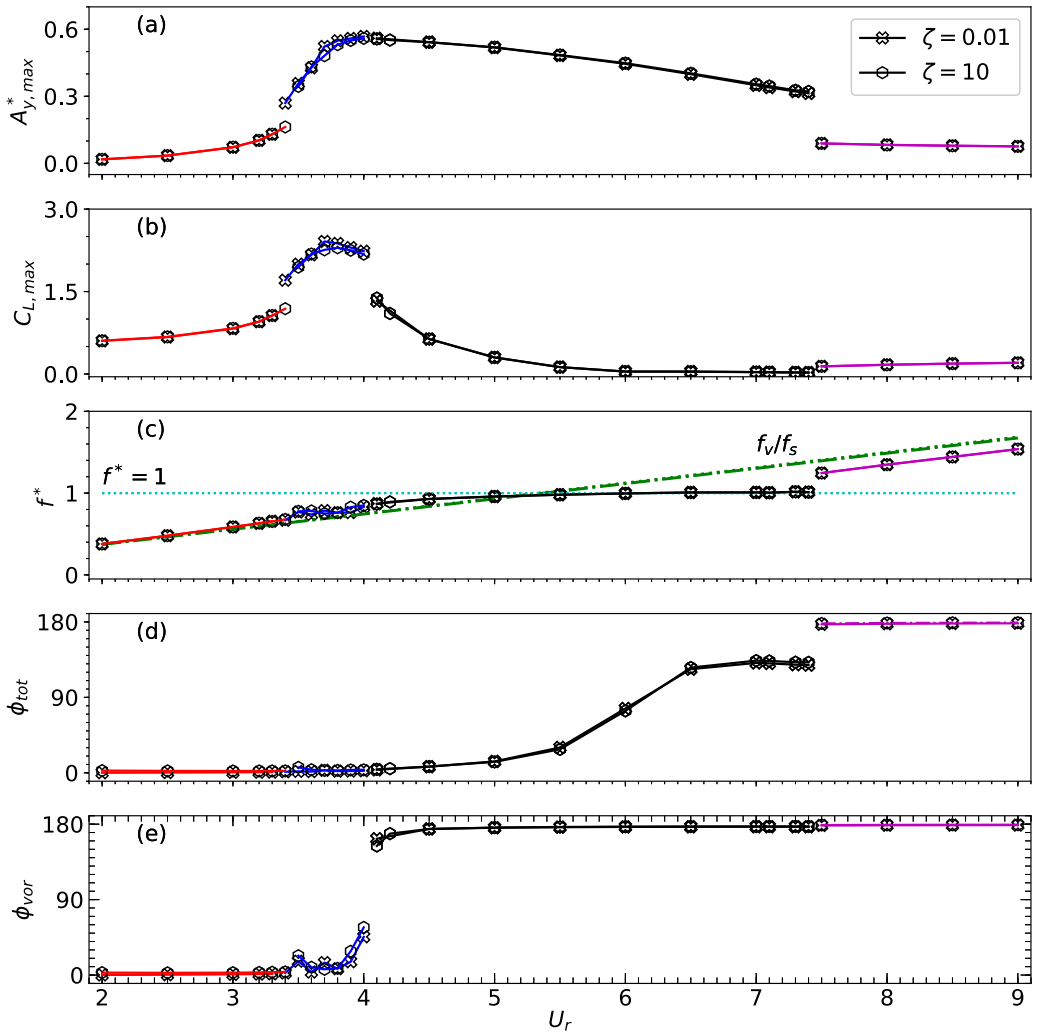

Fig. 19. Comparison for the response for the vibrating cylinder at $\zeta = 0.01$ and $\zeta = 10$: (a) Amplitude; (b) peak lift coefficient; (c) normalized frequency (green line represents the vortex-shedding frequency for a stationary cylinder); (d) mean phase difference between lift and displacement; (e) mean phase difference between vortex force and displacement. (For interpretation of the references to colour in this figure legend, the reader is referred to the web version of this article.)

4.1.4. The Griffin plot

The variation of maximum amplitude with mass and damping ratio is an important design parameter expressed through the *Griffin plot*. Griffin (1980) plotted the peak vibration amplitude of circular cylinder with the product of mass and damping ratio ($m^*\zeta$). Khalak and Williamson (1999) plotted the Griffin plot in terms of $A^*_{y,max}$ and $(m^* + C_A)\zeta$, which becomes important of low mass ratios. Here C_A is added mass coefficient of a circular cylinder. The plot gives a clear functional relationship between them. For the classical spring–damper VIV system, the plot of peak vibration amplitude versus the mass-damping parameter is an exponentially decaying function (Khalak and Williamson, 1999). In Fig. 25, peak vibration amplitude corresponding to an SLS mounted cylinder is plotted against the mass-damping parameter, $(m^* + C_A)\zeta$. The plot shows the maximum amplitude is symmetric about $(m^* + C_A)\zeta \approx 1$. At a very low value of damping ratio, the amplitude is 0.58. As the damping is increased, the amplitude decreases slowly initially and then it decreases at a faster rate, as evident from the steeper variation towards $(m^* + C_A)\zeta = 1$. On further increasing the damping beyond $(m^* + C_A)\zeta = 1$, it mirrors this behaviour again increasing to a maximum value (0.58). The logarithmic x-axis shows that there is a rapid decrease in amplitude with an increase of ζ, whereas the growth of amplitude with ζ beyond $(m^* + C_A)\zeta > 1$ is slower. Though the equivalent frequency is different at the extremes of the damping ratio ($\zeta = 0, \zeta \to \infty$), the maximum amplitude of vibration remains the same. For $\zeta = 0$, the frequency $f_{\zeta=0} = \sqrt{k/m}$, whereas for $\zeta \to \infty$ and $R = 1$, $f_{\zeta\to\infty} = \sqrt{2k/m}$. Clearly, $f_{\zeta\to\infty} = \sqrt{(2)}f_{\zeta=0}$ and the maximum amplitude is 0.58 for both cases. Thus, as expected, the maximum amplitude is not frequency dependent.

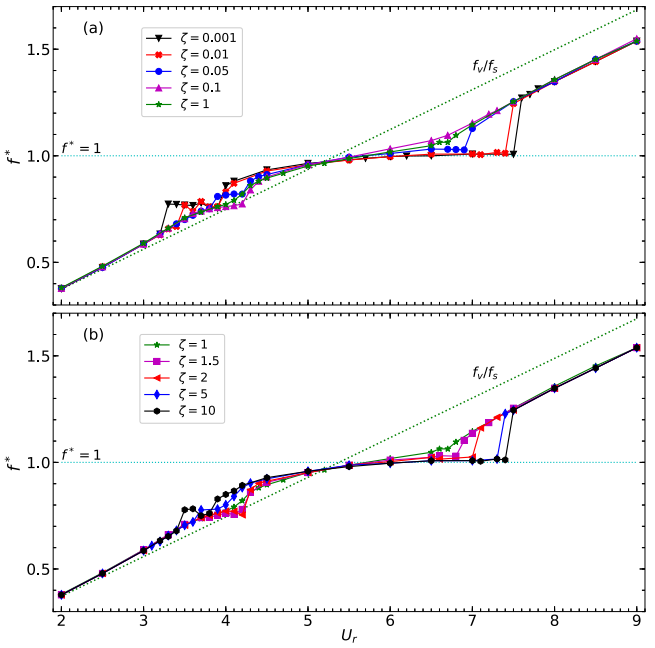

Fig. 20. Comparison of normalized frequency, $f^* = f_y/f_s$, with various damping ratio. The green dotted line represent the vortex-shedding frequency for the stationary cylinder. (For interpretation of the references to colour in this figure legend, the reader is referred to the web version of this article.)

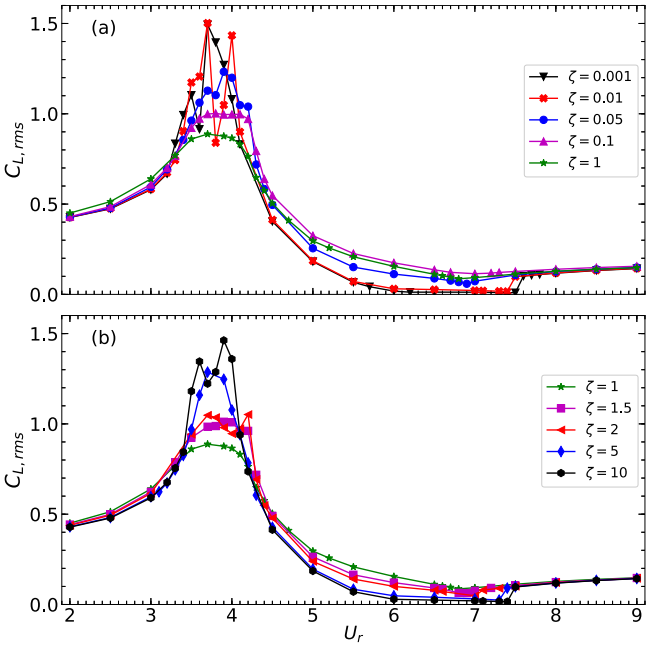

Fig. 21. Response of the mounted cylinder in term of RMS of lift force ($C_{L,rms}$) versus reduced velocity, for damping ratios in the range $\zeta = [0.001, 10]$. Here, $R = 1$.

4.2. Effect of stiffness ratio on the cylinder response at the critical damping ratio

The effect of spring constant ratio R is shown in Fig. 26. Fig. 26(a) shows the amplitude response curves for $R = 0.001, 0.1, 0.5, 1, 2, 10$, for a fixed damping ratio of $\zeta = 1$. For this component of the study, a damping ratio of unity has been chosen because for extreme values of ζ the structural system behaves as a purely elastic system. This choice

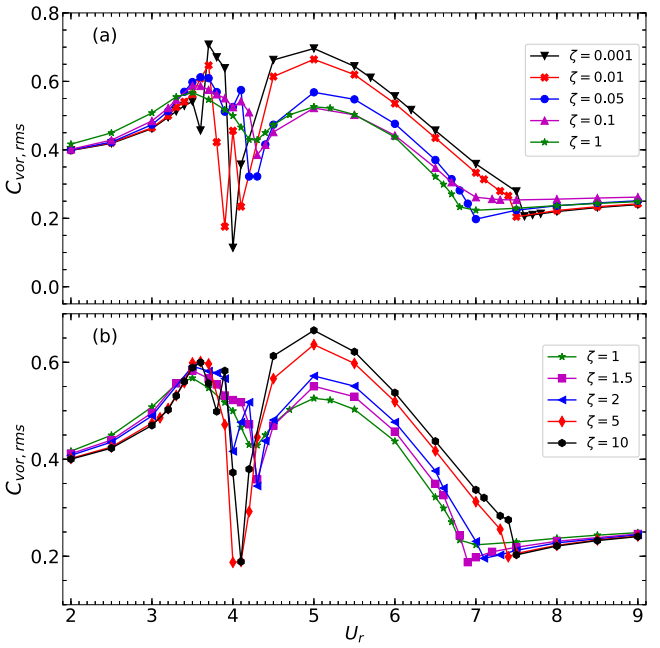

Fig. 22. Response for the mounted cylinder by comparing the RMS of the vortex force ($C_{vor,rms}$) with reduced velocity, for damping ratio $\zeta = [0.001 - 10]$ and $R = 1$.

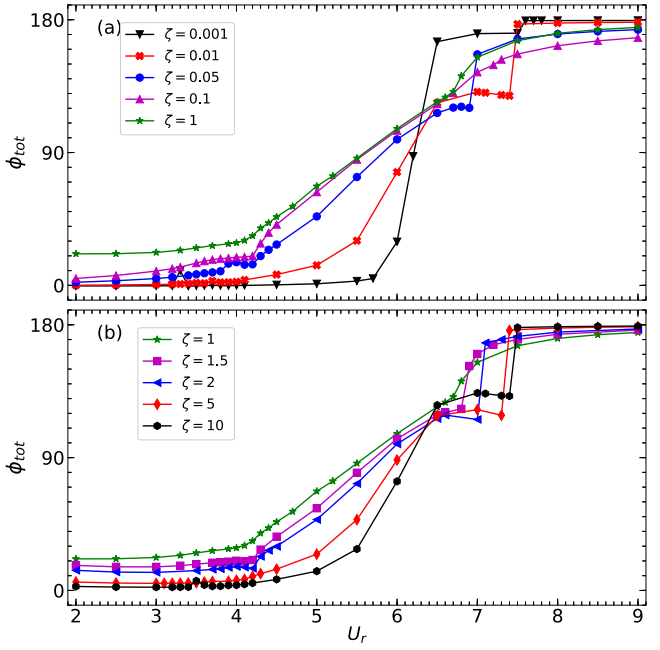

Fig. 23. Response for the mounted cylinder by comparing the mean phase difference of the lift force and cylinder displacement versus reduced velocity, for damping ratio $\zeta = [0.001 - 10]$, $R = 1$.

incorporates the maximal damping effect for the $R = 1$ case. It is observed that the amplitude response on increasing R is similar to that observed for increasing ζ for $\zeta < 1$. As shown in Fig. 26(a), the vibration amplitude decreases with an increase in R for all values of the reduced velocity. For $R = 0.01, 0.1, 0.5$, there is a sudden jump in the peak of lift force (refer to Fig. 26(b)), which may help to demarcate the initial, upper-type and lower-type branches, as explained in the previous section. The initial to upper-type branch jump is clearly visible for $R = 0.01, 0.1$ in the normalized frequency and vortex phase-difference plots given in Fig. 27.

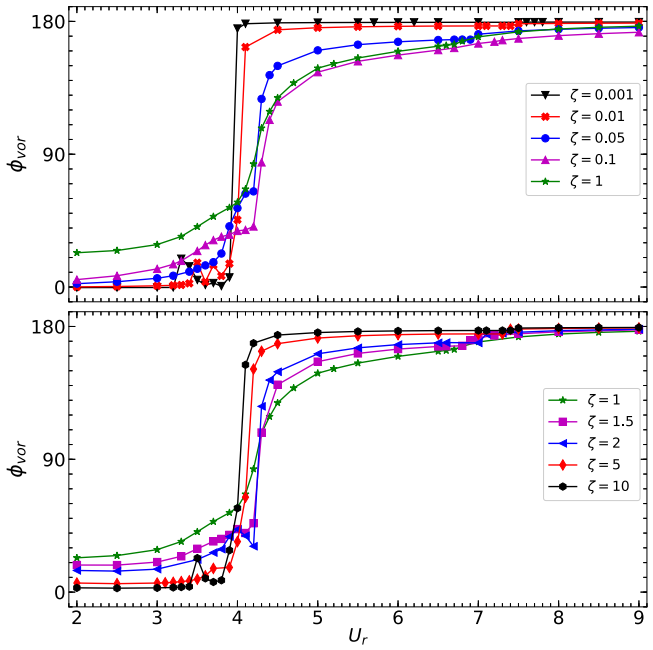

Fig. 24. Response for the mounted cylinder by comparing the mean phase difference of the vortex force and cylinder displacement versus reduced velocity, for damping ratio, $\zeta = [0.001 - 10]$, $R = 1$.

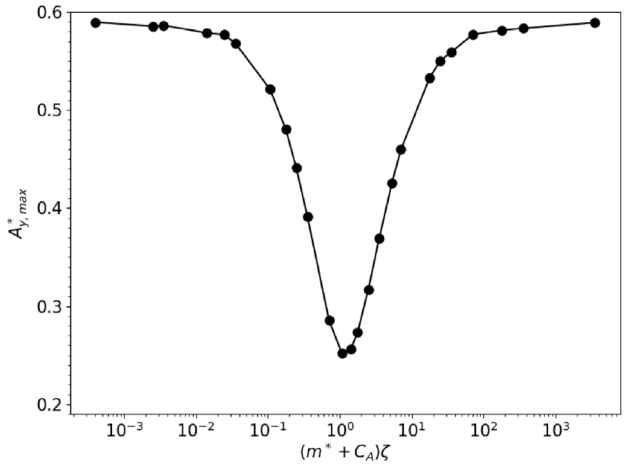

Fig. 25. Griffin plot of the peak amplitude data against logarithm of the mass-damping parameter, $(m^* + C_A)\zeta$ for $R = 1$.

It is observed in Figs. 26 and 27(a) that there is a delay in the jump from the initial to upper-type branch as R is increased. The jump corresponding to $R = 0.01$ occurs at $U_r = 3.3$, whereas it occurs at $U_r = 3.4$ for $R = 0.1$. There is also an earlier start of desynchronization with an increase in R. The delay in the jump from initial to upper-type branch and earlier entry into the desynchronization region with R shorten the lock-in region; which is clearly visible in Fig. 27(a). There is barely any distinguishable lock-in for $R > 2$. This behaviour is expected, as, for the very low values of R, the SLS mechanism converts to a single spring elastic system, similar to the situation for very low values of ζ, which also becomes effectively a single spring elastic system. For a very high value of R, the SLS mechanism becomes a classical spring–damper in parallel (refer to Fig. 4(c)). This system (Fig. 4(c)) with considerable damping $\zeta = 1$ will show strongly reduced vibration without jumps between transitions. As R is increased, the change in phase difference between different branches become more continuous and tends to reduce (refer to Fig. 27(b,c)). The difference is no longer 0° or 180°, and takes intermediate values as the reduced velocity is varied. Setting R to a high value effectively corresponds to a change from the SLS to the Kelvin-Voigt model – the classical damped VIV system. As shown by Soti et al. (2018) and Klamo et al. (2006), the vibration amplitude decreases with damping for the Kelvin-Voigt model for a damped VIV system.

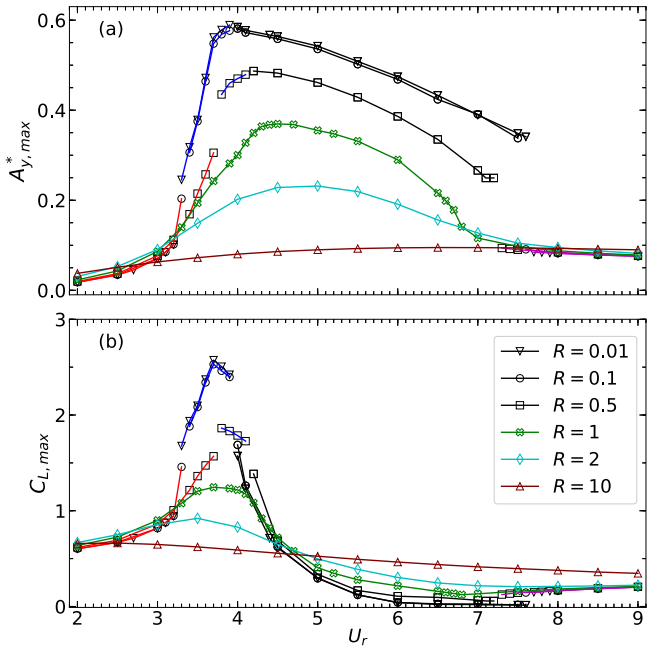

Fig. 26. Response of the cylinder for varying spring stiffness ratio $R = [0.001 - 10]$ at $Re = 150$, $\zeta = 1$ and $m^* = 2.546$: variation of (a) $A^*_{y,max}$, (b) $C_{L,max}$, versus reduced velocity (U_r).

5. Conclusions

The effect of a viscoelastic-type structural support on the response of vortex-induced vibration (VIV) of a circular cylinder has been investigated numerically using a spectral-element based FSI solver, for mass ratio $m^* = 2.546$ at $Re = 150$. A survey of the literature indicates that the effect of this type of SLS spring–damper system on VIV has received little attention, even through the mechanism allows further control on enhancing or suppressing the VIV response. The spring–damper system used to provide viscoelastic support is similar to the Standard Linear Solid (SLS) model, consisting a spring together with a spring–damper combination connected in parallel. This response is governed by two parameters: the damping ratio, ζ, and spring constant ratio, R. The amplitude response of cylinder vibration is calculated at different reduced velocities by varying these parameters. In this case, the reduced velocity, U_r, is calculated based on the natural frequency of the system taking into consideration the damping. The maximum amplitude is calculated as ζ and R are varied. In particular, the effect of structural damping was determined for $\zeta = 0.001, 0.01, 0.05, 0.1, 1, 2, 5$ and 10, over the range of U_r covering the main resonant response. It is found that for very low values of ζ (=0.001), two regimes of synchronized response exist, which show resemblance to the upper and lower branches observed in higher Reynolds number experiments. These regimes are referred to as the upper-type and lower-type branches. As there is no clear jump in vibration amplitude at the transition, evidence for these separate branches comes from a jump in the magnitude of peak lift forces, oscillation frequency and phase difference between the vortex force and vibration displacement. In addition, an initial branch is observed. This is associated with vibration frequencies close to vortex-shedding frequency of stationary cylinder, a monotonic increase in the RMS lift coefficient and vortex force, and total- and vortex-phase difference 0°. At higher reduced velocity, the upper-type branch is characterized by the jump in peak lift force, reduced periodicity, and zig-zag variation of RMS of lift coefficient and vortex force, a jump in vibration frequency to be close to the natural frequency of the structural system, a total phase difference 0° and a jump in vortex phase difference at the start of branch. Beyond this, transition to the lower-type branch is defined by a jump in peak lift force, constant vibration frequency remaining close to the natural frequency of the system, and total phase difference $\sim 180°$. As damping is increased, the initial branch increases and identification of the upper-type branch becomes difficult. On further increasing ζ beyond $\zeta > 1$, a higher amplitude response is again observed.

Indeed, the effect of varying ζ shows that there is a critical damping ratio at $(m^* + C_A)\zeta \approx 1$ about which similar behaviour is seen as ζ is either decreased or increased from this point. The predictions show that for $(m^* + C_A)\zeta < 1$ on increasing damping, the amplitude decreases from a maximum of $0.58D$ to $0.25D$, whereas on further increasing damping above $(m^* + C_A)\zeta > 1$, the amplitude again increases asymptotically towards $0.58D$. This non-monotonic variation of amplitude with damping is a characteristic of the SLS model, which tends towards a purely elastic system at very low and very high values of damping ratio. The effect of damping on the peak vibration amplitude is quantified in the *Griffin* plot. This plot of peak amplitude against mass-damping parameter shows a *well-shaped* curve, distinctly different to that seen for the classical (Kelvin-Voigt) VIV system.

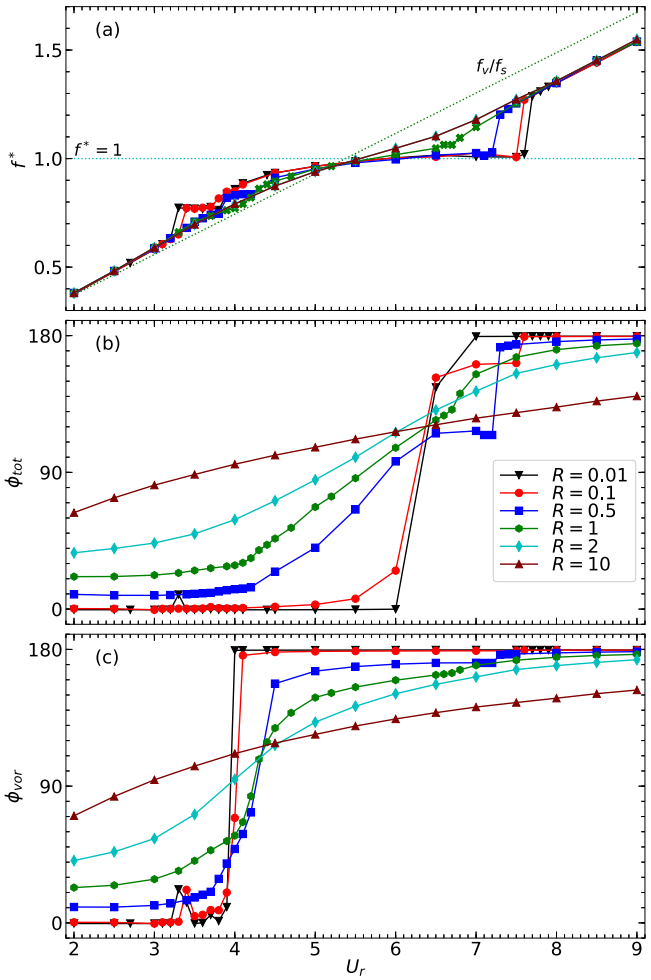

Fig. 27. (a) Variation of normalized frequency (f^*) versus reduced velocity (U_r)). The green dotted line represents the vortex-shedding frequency of a stationary cylinder. (b) The variation of phase difference between vortex force and cylinder displacement (ϕ_{vor}) versus U_r). (For interpretation of the references to colour in this figure legend, the reader is referred to the web version of this article.)

The effect of varying R was also studied for $R = 0.01, 0.1, 0.5, 1, 2$ and 10 at $\zeta = 1$, and shows that the maximum amplitude of vibration decreases as R is increased. For a very low value of $R = 0.01$, an upper-type branch exists. For larger values of R, the amplitude of the cylinder vibration becomes very small and does not show distinct branches of cylinder response. High values of R effectively convert the SLS model to the Kelvin-Voigt model (i.e. the classical spring–damper VIV system), where the vibration amplitude decreases with increased damping.

The present results suggest that it may be possible to tune the behaviour of a structural system by actively modifying the damping. This approach could be potentially exploited for applications that require control of VIV. It could allow tuning of damping to generate large amplitude oscillations, while in other cases where VIV is detrimental oscillations could be suppressed.

Declaration of competing interest

The authors declare that they have no known competing financial interests or personal relationships that could have appeared to influence the work reported in this paper.

CRediT authorship contribution statement

Rahul Mishra: Conceptualization, Software, Investigation, Writing - original draft . **Atul Soti:** Software, Writing - review & editing. **Rajneesh Bhardwaj:** Writing - review & editing. **Salil S. Kulkarni:** Writing - review & editing. **Mark C. Thompson:** Software, Writing - review & editing.

Acknowledgements

Support from computing time allocations from the Pawsey Supercomputing Centre with funding from the Australian Government is strongly acknowledged. R.B. gratefully acknowledges the financial support of a CSR grant from Portescap Inc., India, and of an internal grant from Industrial Research and Consultancy Centre (IRCC), IIT Bombay.

References

Bao, Y., Huang, C., Zhou, D., Tu, J., Han, Z., 2012. Two-degree-of-freedom flow-induced vibrations on isolated and tandem cylinders with varying natural frequency ratios. J. Fluids Struct. 35, 50–75.
Bearman, P.W., 1984. Vortex shedding from oscillating bluff bodies. Annu. Rev. Fluid Mech. 16 (1), 195–222.
Bearman, P., 2011. Circular cylinder wakes and vortex-induced vibrations. J. Fluids Struct. 27 (5–6), 648–658.
Blackburn, H., Henderson, R., 1996. Lock-in behavior in simulated vortex-induced vibration. Exp. Therm Fluid Sci. 12 (2), 184–189.
Blevins, R.D., Coughran, C.S., 2009. Experimental investigation of vortex-induced vibration in one and two dimensions with variable mass, damping, and reynolds number. J. Fluids Eng. 131 (10), 101202.
Brika, D., Laneville, A., 1993. Vortex-induced vibrations of a long flexible circular cylinder. J. Fluid Mech. 250, 481–508.
de Lima, A., da Cunha, B., da Silva, A., Rodovalho, L., 2018. Vortex-induced vibration analysis of viscoelastically mounted rigid circular cylinders in cross-flow at a moderate reynolds number. J. Vib. Control 24 (13), 2688–2700.
Feng, C., 1968. The Measurement of Vortex Induced Effects in Flow Past Stationary and Oscillating Circular and D-Section Cylinders (Ph.D. thesis). University of British Columbia.
Findley, W.N., Davis, F.A., 2013. Creep and Relaxation of Nonlinear Viscoelastic Materials. Courier Corporation.
Govardhan, R., Williamson, C., 2000. Modes of vortex formation and frequency response of a freely vibrating cylinder. J. Fluid Mech. 420, 85–130.
Griffin, O., 1980. Vortex-excited cross-flow vibrations of a single cylindrical tube. J. Press. Vessel Technol. 102 (2), 158–166.
Gsell, S., Bourguet, R., Braza, M., 2016. Two-degree-of-freedom vortex-induced vibrations of a circular cylinder at Re= 3900. J. Fluids Struct. 67, 156–172.
Guilmineau, E., Queutey, P., 2004. Numerical simulation of vortex-induced vibration of a circular cylinder with low mass-damping in a turbulent flow. J. Fluids Struct. 19 (4), 449–466.
Hourigan, K., Thompson, M., Tan, B., 2001. Self-sustained oscillations in flows around long blunt plates. J. Fluids Struct. 15 (3–4), 387–398.
Karniadakis, G.E., Israeli, M., Orszag, S.A., 1991. High-order splitting methods for the incompressible Navier-Stokes equations. J. Comput. Phys. 97 (2), 414–443.
Karniadakis, G., Sherwin, S., 2013. Spectral/Hp Element Methods for Computational Fluid Dynamics. Oxford University Press.
Khalak, A., Williamson, C., 1997. Fluid forces and dynamics of a hydroelastic structure with very low mass and damping. J. Fluids Struct. 11 (8), 973–982.
Khalak, A., Williamson, C.H., 1999. Motions, forces and mode transitions in vortex-induced vibrations at low mass-damping. J. Fluids Struct. 13 (7–8), 813–851.
Klamo, J., Leonard, A., Roshko, A., 2005. On the maximum amplitude for a freely vibrating cylinder in cross-flow. J. Fluids Struct. 21 (4), 429–434.
Klamo, J., Leonard, A., Roshko, A., 2006. The effects of damping on the amplitude and frequency response of a freely vibrating cylinder in cross-flow. J. Fluids Struct. 22 (6–7), 845–856.
Lee, H., Hourigan, K., Thompson, M.C., 2013. Vortex-induced vibration of a neutrally buoyant tethered sphere. J. Fluid Mech. 719, 97–128.
Leontini, J.S., Jacono, D.L., Thompson, M.C., 2011. A numerical study of an inline oscillating cylinder in a free stream. J. Fluid Mech. 688, 551–568.
Leontini, J., Stewart, B., Thompson, M., Hourigan, K., 2006a. Wake state and energy transitions of an oscillating cylinder at low reynolds number. Phys. Fluids 18 (6), 067101.
Leontini, J., Thompson, M., Hourigan, K., 2006b. The beginning of branching behaviour of vortex-induced vibration during two-dimensional flow. J. Fluids Struct. 22 (6–7), 857–864.
Mishra, R., Kulkarni, S.S., Bhardwaj, R., Thompson, M.C., 2019. Response of a linear viscoelastic splitter plate attached to a cylinder in laminar flow. J. Fluids Struct. 87, 284–301.
Mittal, S., et al., 2017. A new regime of multiple states in free vibration of a cylinder at low Re. J. Fluids Struct. 68, 310–321.
Pan, Z., Cui, W., Miao, Q., 2007. Numerical simulation of vortex-induced vibration of a circular cylinder at low mass-damping using RANS code. J. Fluids Struct. 23 (1), 23–37.
Parkinson, G., 1989. Phenomena and modelling of flow-induced vibrations of bluff bodies. Prog. Aerosp. Sci. 26 (2), 169–224.
Pastrana, D., Cajas, J., Lehmkuhl, O., Rodríguez, I., Houzeaux, G., 2018. Large-eddy simulations of the vortex-induced vibration of a low mass ratio two-degree-of-freedom circular cylinder at subcritical reynolds numbers. Comput. & Fluids 173, 118–132.
Rajamuni, M.M., Thompson, M.C., Hourigan, K., 2018. Transverse flow-induced vibrations of a sphere. J. Fluid Mech. 837, 931–966.
Sarpkaya, T., 1979. Vortex-induced oscillations: a selective review. J. Appl. Mech. 46 (2), 241–258.
Sarpkaya, T., 2004. A critical review of the intrinsic nature of vortex-induced vibrations. J. Fluids Struct. 19 (4), 389–447.
Scruton, C., 1963. On the wind excited oscillations of stacks, towers and masts. In: Proc. Int. Conf. Wind Effects on Buildings and Structures (Teddington), pp. 798–833.
Sheard, G.J., Thompson, M.C., Hourigan, K., 2003. From spheres to circular cylinders: the stability and flow structures of bluff ring wakes. J. Fluid Mech. 492, 147–180.
Soti, A.K., Thompson, M.C., Sheridan, J., Bhardwaj, R., 2017. Harnessing electrical power from vortex-induced vibration of a circular cylinder. J. Fluids Struct. 70, 360–373.
Soti, A.K., Zhao, J., Thompson, M.C., Sheridan, J., Bhardwaj, R., 2018. Damping effects on vortex-induced vibration of a circular cylinder and implications for power extraction. J. Fluids Struct. 81, 289–308.
Sumer, B.M., et al., 2006. Hydrodynamics around Cylindrical Strucures, Vol. 26. World scientific.
Thompson, M.C., Hourigan, K., Cheung, A., Leweke, T., 2006. Hydrodynamics of a particle impact on a wall. Appl. Math. Model. 30 (11), 1356–1369.
Thompson, M., Hourigan, K., Sheridan, J., 1996. Three-dimensional instabilities in the wake of a circular cylinder. Exp. Therm Fluid Sci. 12 (2), 190–196.
Vickery, B., Watkins, R., 1964. Flow-induced vibrations of cylindrical structures. In: Hydraulics and Fluid Mechanics. Elsevier, pp. 213–241.
Wang, E., Xiao, Q., Incecik, A., 2017. Three-dimensional numerical simulation of two-degree-of-freedom VIV of a circular cylinder with varying natural frequency ratios at Re= 500. J. Fluids Struct. 73, 162–182.
Williamson, C., Govardhan, R., 2004. Vortex-induced vibrations. Annu. Rev. Fluid Mech. 36, 413–455.
Williamson, C., Govardhan, R., 2008. A brief review of recent results in vortex-induced vibrations. J. Wind Eng. Ind. Aerodyn. 96 (6–7), 713–735.
Williamson, C.H., Roshko, A., 1988. Vortex formation in the wake of an oscillating cylinder. J. Fluids Struct. 2 (4), 355–381.
Wu, X., Ge, F., Hong, Y., 2012. A review of recent studies on vortex-induced vibrations of long slender cylinders. J. Fluids Struct. 28, 292–308.
Zhao, M., 2013. Flow induced vibration of two rigidly coupled circular cylinders in tandem and side-by-side arrangements at a low reynolds number of 150. Phys. Fluids 25 (12), 123601.